Research and Development Technical Report
CECOM-TR-92-B007-F

# A CASCADABLE, MONOLITHIC LASER/ MODULATOR/AMPLIFIER TRANSMITTER

Dr. Stephen R. Forrest

Princeton University
Advanced Techology Center for Photonics and Optoelectronic Materials
Princeton, New Jersey 08544

March 1997

DISTRIBUTION STATEMENT

Approved for public release; distribution is unlimited.

19970515 028

**CECOM**
**U.S. ARMY COMMUNICATIONS-ELECTRONICS COMMAND**
**RESEARCH, DEVELOPMENT AND ENGINEERING CENTER**
**FORT MONMOUTH, NEW JERSEY 07703-5203**

DTIC QUALITY INSPECTED 1

# NOTICES

## Disclaimers

The findings in this report are not to be construed as an official Department of the Army position, unless so designated by other authorized documents.

The citation of trade names and names of manufacturers in this report is not to be construed as official Government endorsement or approval of commercial products or services referenced herein.

# REPORT DOCUMENTATION PAGE

*Form Approved*
*OMB NO. 0704-0188*

Public reporting burden for this collection of information is estimated to average 1 hour per response, including the time for reviewing instructions, searching existing data sources, gathering and maintaining the data needed, and completing and reviewing the collection of information. Send comment regarding this burden estimates or any other aspect of this collection of information, including suggestions for reducing this burden, to Washington Headquarters Services. Directorate for information Operations and Reports, 1215 Jefferson Davis Highway, Suite 1204, Arlington, VA 22202-4302, and to the Office of Management and Budget, Paperwork Reduction Project (0704-0188), Washington, DC 20503.

1. AGENCY USE ONLY *(Leave blank)*

2. REPORT DATE
March 1997

3. REPORT TYPE AND DATES COVERED
Final Report: Sep 92 to Sep 96

4. TITLE AND SUBTITLE
A CASCADABLE, MONOLITHIC LASER/MODULATOR/AMPLIFIER TRANSMITTER

5. FUNDING NUMBERS
C: DAAB07-92-C-B007
PE: 611102

6. AUTHOR(S)
Dr. Stephen R. Forrest

7. PERFORMING ORGANIZATION NAMES(S) AND ADDRESS(ES)
Princeton University
Advanced Technology Center for Photonics and Optoelectronic Materials
Princeton, NJ 08544

8. PERFORMING ORGANIZATION REPORT NUMBER

9. SPONSORING / MONITORING AGENCY NAME(S) AND ADDRESS(ES)
US Army Communications-Electronics Command (CECOM)
Space and Terrestrial Communications Directorate
ATTN: AMSEL-RD-ST-SY-TE (J. Wright)
Fort Monmouth, NJ 07703-5203

10. SPONSORING / MONITORING AGENCY REPORT NUMBER
CECOM-TR-92-B007-F

11. SUPPLEMENTARY NOTES
Space and Terrestrial Communications Directorate Project Engineer: James G. Wright, (908) 427-2819.

12a. DISTRIBUTION / AVAILABILITY STATEMENT
Approved for public release; distribution is unlimited.

12 b. DISTRIBUTION CODE

13. ABSTRACT *(Maximum 200 words)*

High performance devices were designed and fabricated based on gas source molecular beam epitaxially (GSMBE) grown InGaAsP. These included low threshold, strained InGaAsP multiple quantum well (MQW) Fabry Perot lasers which exhibited the lowest threshold current densities ever achieved for GSMBE grown material operating at 1.3 um; very high on/off ratio (40 dB) Mach-Zehnder modulators and high gain (25 dB) semiconductor optical amplifiers. These devices were developed to demonstrate the integration of multifunctional photonic integrated circuits employing one or more of these devices in any combination needed for a given application. This led to a demonstration of a very simple and flexible integration technology based on a modified twin waveguide structure which completely eliminated complicated regrowth processing.

14. SUBJECT TERMS
Surface-emitting lasers; Mach-Zehnder modulators; gas source molecular beam epitaxy; optoelectronic integrated circuit; indium gallium arsenic phosphide; semiconductor optical amplifier

15. NUMBER IF PAGES
50

16. PRICE CODE

| 17. SECURITY CLASSIFICATION OF REPORT | 18. SECURITY CLASSIFICATION OF THIS PAGE | 19. SECURITY CLASSIFICATION OF ABSTRACT | 20. LIMITATION OF ABSTRACT |
|---|---|---|---|
| Unclassified | Unclassified | Unclassified | UL |

# Table of Contents

Foreword.....2

Final Report.....3

Publications Made Possible in Part to Support from this Program.....5

Personnel Supported Under this Contract.....7

Appendices:

A1. Growth of abrupt InGaAs(P)/In(GaAs)P heterointerfaces by gas source molecular beam epitaxy.....8

A2. Low-Threshold, High-Power, 1.3-µm Wavelength, InGaAsP-InP Etched-Facet Folded-Cavity Surface-Emitting Lasers.....14

A3. Low-threshold 1.3-µm wavelength, InGaAsP strained-layer multiple quantum well lasers grown by gas source molecular beam epitaxy.....18

B. Fabrication and Analysis of High Contrast InGaAsP-InP Mach-Zehnder Modulators for Use at 1.55-µm Wavelength.....21

C. Monolithic Integration of an InGaAsP/InP MQW Laser/Waveguide Using a Twin-Guide Structure with a Mode Selection Layer.....24

D. Technologies for Large Scale InP-based Optoelectronic Integrated Circuits.....39

# Foreword

Within the framework of the contract effort, much of the substance was reported in the publications which comprise the appendices to this report. As a consequence, the initial text of the report is a briefly stated synposis which summarizes the overall contract efforts.

# A CASCADABLE, MONOLITHIC LASER/MODULATOR/AMPLIFIER TRANSMITTER

**Principal Investigator:** Stephen R. Forrest
Center for Photonics and Optoelectronic Materials
Department of Electrical Engineering
Princeton University
Princeton, NJ 08544
(609) 258-4532

**Contract No.:** DAAB07-92-C-B007

## Final Report

During the course of this program, we demonstrated several extremely high performance devices based on gas source molecular beam epitaxially grown InGaAsP. Among those devices, we report the following results:

- Low threshold, strained InGaAsP MQW Fabry Perot lasers. These devices exhibited the lowest threshold current densities ever achieved for GSMBE grown material operating at a wavelength of 1.3 µm. This result was a direct consequence of our ability to grow atomically abrupt heterointerfaces using a novel growth method. (See Appendix A)
- Very high on/off ratio (40 dB) Mach-Zehnder MQW modulators. (See Appendix B)
- High gain (25dB) semiconductor optical amplifiers.

All of these devices were designed and fabricated such that we could demonstrate the integration of multifunctional photonic integrated circuits (PICs) employing one or more of these devices in any combination needed for a given application. This led to our demonstration of a very simple, and flexible integration technology based on a modified twin waveguide (TG) structure (see Appendix C). We developed this TG technology to completely eliminate

complicated regrowth processing, such that we can ultimately realize an integration "platform" whereby any combination of active (i.e. SOAs, lasers) and passive (i.e. waveguides, modulators) optical devices can be arbitrarily combined with different PICs on a single, multipurpose wafer structure.

The basic concept of the TG structure is that an active MQW region is grown above a passive waveguide/modulator region, separated by an intermediate "cladding" region. A laser or SOA is then defined in the active region by etching down into the clad. The difference between these two devices is simply the facet reflectivity: an SOA has anti-reflection coated facets, whereas a laser has high reflection coatings. To realize this device, we also needed to develop very high quality facet formation processes based on $CH_4$:$H_2$ reactive ion etching.

The light generated in the active region is evanescently coupled into the passive, or waveguide region located directly below. As in any directional coupler, the coupling efficiency is a sensitive function of length. For this reason, previous results for such TG structures report a maximum coupling efficiency of 13%. To eliminate this length dependence, hence making the TG a practical integration scheme for the first time, we grew a thin (~100Å-500Å) InGaAs absorbing, or "loss" layer in the center of the intermediate InP cladding layer. This loss layer is grown since we recognize that the length dependence of the coupling arises from an interplay between the odd and even modes propagating in the structure. Due to the different effective indices of these two modes, their velocities are different, and hence they are in and out of phase at different positions within the active cavity. The loss layer effectively eliminates the even mode, hence eliminating this energy exchange with its concomitant length dependence.

Using our modified TG structure, we find that we completely eliminate the even mode, resulting in complete elimination of any length dependence in the strucuture. *Furthermore, in our first test device (a laser coupled to a waveguide Y-junction) we measured a 50% coupling between the laser and the waveguide. This is equal to the theoretical maximum coupling allowed in this structure, far exceeding all previous reports for coupling efficiency in such integrated devices.*

Hence, the TG structure with loss layer developed under this program (and detailed further in the preprint attached) provides a radical new approach to integrating passive and active optical devices on a single epitaxial wafer structure. Hence, we succeeded in this program in demonstrating a practical "platform" PIC technology which is free from sensitivity to fabrication and epitaxial growth variations, and does not employ highly complex and costly regrowth methods. For the first time, we can look forward to generating a wide range of PICs on a single wafer, similar to what is accomplished using a single Si wafer to generate a wide range of integrated circuits and codes.

**Publications Made Possible in Part to Support from this Program:**


1. "Low Threshold 1.3 μm Wavelength, InGaAsP Strained-Layer Multiple Quantum Well Lasers Grown by Gas Source Molecular Beam Epitaxy", G-J. Shiau, C-P. Chao, P. E. Burrows, and S. R. Forrest, *Appl. Phys. Lett.*, **65**, 892 (1994).

2. "Growth of abrupt InGaAs(P)/In(GaAs)P Heterointerfaces by Gas Source Molecular Beam Epitaxy", G.-J. Shiau, C-P. Chao, P. E. Burrows and S. R. Forrest, *J. Appl. Phys.*, **77**, 201 (1995).

3. "1.3 μm Wavelength, InGaAsP/InP Folded-Cavity Surface-Emitting Lasers Grown by Gas Source Molecular Beam Epitaxy", C-P Chao, G-J Shiau and S. R. Forrest, *IEEE Photonics Technology Lett.*, **6**, 1406 (1994).

4. "Photoluminscence Study of Excess Carrier Spillover in 1.3μm Wavelength Strained Multi-Quantum Well InGaAsP/InP Laser

Structures", D. Garbuzov, G-J Shiau, V. Bulovic, M. Boroditsky, C-P Chao and S. R. Forrest, *Appl. Phys. Lett.*, **66** 1307 (1995).

4. "Low Threshold, High Power, 1.3μm Wavelength, InGaAsP/InP Etched-Facet Folded-Cavity Surface-Emitting Lasers", C-P Chao, D. G. Garbuzov, G-J Shiau and S. R. Forrest, *IEEE Photonics Technology Lett.*, **7**, 836 (1995)

6. "Fabrication and Analysis of High Contrast InGaAsP/InP Mach-Zehnder Modulators for Use at 1.55μm Wavelength", M. Fetterman, C-P Chao and S. R. Forrest, *IEEE Photonics Technology Lett.*, **8**, 69 (1995).

7. "Modelling of a waveguide device using the Helmholtz beam propagation method", M. R. Fetterman and S. R. Forrest, *Top. Mtg. on Integrated Photonics Research*, Paper ThD4, San Francisco (Feb., 1994).

8. "A novel growth interruption sequence for improved heterointerface quality during growth of In(GaAs)P/InGaAs by gas source MBE", G-J Shiau, P. E. Burrows and S. R. Forrest, *Materials Research Society Spring Mtg.*, San Francisco (April, 1994)

9. "Low Threshold 1.3 μm InGaAsP/InP Strained-Layer Multiple Quantum Well Lasers Grown by Gas Source Molecular Beam Epitaxy", G.-J. Shiau, C-P Chao, P. E. Burrows and S. R. Forrest, Paper E7, *Electron. Mat. Conf.*, Boulder, CO (June, 1994).

10. "1.3μm Wavelength, Folded-Cavity Surface Emitting Lasers Fabricated by CH4/H2 Angled Facet Reactive Ion Etching", C. P. Chao, G.-J. Shiau and S. R. Forrest, *IEEE-LEOS Annual Meeting*, Paper SL5.5, Boston (Oct., 1994).

11. "1.3μm Wavelength, InGaAsP/InP Etched-Facet Folded-Cavity Surface Emitting Lasers for Photonic Integration", C-P Chao, G-J Shiau, D Garbuzov and S. R. Forrest, *Integrated Photonic Research Conf.*, Paper IFA5, Dana Point, CA (Jan., 1995).

12. "Photonic Integrated Circuits for Phased Array Antenna Systems", C.P. Chao, G. J. Shiau, M. Fetterman and S. R. Forrest, *PSAA-V*, Monterey CA (Jan., 1995).

13. "Photoluminescence Study of Excess Carrier Spillover in 1.3μm Wavelength Strained Multiple Quantum Well InGaAsP/InP Laser Structures", D. Garbuzov, G-J Shiau, V. Bulovic, M. Boroditsky, C-P Chao and S. R. Forrest, *CLEO '95*, paper CTuL2, Baltimore (May, 1995).

14. "Sources and Circuits for High Performance Smart-Pixel Based Optoelectronic Interconnections", S. R. Forrest, K. Beyzavi, D. S. Kim, G. J. Shiau and C. P. Chao, *Conf. on Lasers and Electro-Optics '95*, invited, EOS 3.3, p.270, San Francisco (Oct., 1995)

15. "Analysis and Fabrication of High-Contrast InGaAsP/InP Mach-Zehnder Modulators for use at 1.55µm Wavelength", M. Fetterman, C-P Chao and S. R. Forrest, *Conf. on Lasers and Electro-Optics '95*, IO 5.3, p.126, San Francisco, (Oct., 1995)

16. "Monolithic Integration of an InGaAsP/InP MQW Laser/Waveguide Using a Twin-Guide Structure with a Mode Selection Layer", L. Xu, M. R. Gokhale, P. Studenkov, J. C. Dries, C.-P. Chao, D. Garbuzov and S. R. Forrest, *IEEE Photonics Technology Lett.*, accepted (1997).

17. "Technologies for Large Scale InP-based Optoelectronic Integrated Circuits", S. R. Forrest, D. S. Kim, S. Yu, J. Thomson, L. Xu, M. Gokhale, J. C. Dries, M. Lange, G. H. Olsen, and M. Cohen, SPIE Conf. on Optoelectronic Integrated Circuits, invited, **3006**, 186, San Jose, CA (Feb., 1997)

18. "Monolithic Integration of Laser and Waveguide Using a Twin-Guide Structure with Absorption Layer", P. Studenkov, M. Gokhale, L. Xu, J. C. Dries, C.-P. Chao, D. Garbuzov and S. R. Forrest, 9th In. Conf. on InP and Related Materials, Hyannis, MA (May, 1997).

**Personnel Supported Under this Contract:**

1. Dr. G-J. Shiau (PhD, 1995): Currently at Applied Materials
2. Dr. C-P Chao (Post-Doc); Currently at Texas Instruments
3. Matthew Fetterman: Currently student of Prof. Warren, Princeton University
4. Dr. D. Garbuzov, Visiting Fellow
5. J. C. Dries (PhD student)

# Growth of abrupt InGaAs(P)/In(GaAs)P heterointerfaces by gas source molecular beam epitaxy

Guang-Jye Shiau, Chih-Ping Chao, Paul E. Burrows, and Stephen R. Forrest
*Advanced Technology Center for Photonics and Optoelectronic Materials, Department of Electrical Engineering, Princeton University, Princeton, New Jersey 08544*

(Received 6 June 1994; accepted for publication 16 September 1994)

We demonstrate a novel method for the growth of abrupt InGaAs(P)/In(GaAs)P heterojunctions by gas source molecular beam epitaxy. We find that exposure of freshly grown InP to an As flux during growth interruption between layers of different compositions results in the substitution of surface P atoms and As atoms, thereby generating a strained transition layer at each interface. By assuring a group-III stabilized surface during interruption required to grow InGaAs(P)/In(GaAs)P heterointerfaces, As/P substitution can be avoided, thereby resulting in improved interface quality. Heterointerface abruptness was examined by double-crystal x-ray diffraction and low temperature photoluminescence. The results show that the interfaces grown with the modified switching sequence are considerably more abrupt than those obtained using conventional sequences where As/P interdiffusion extends over several monolayers. © *1995 American Institute of Physics.*

## I. INTRODUCTION

Growth of high quality heterointerfaces has been a key factor in improving the properties of optoelectronic devices such as multiple quantum well (MQW) lasers and modulators. However, modern gas phase epitaxial techniques, including metalorganic chemical vapor deposition (MOCVD), chemical beam epitaxy (CBE), and gas source molecular beam epitaxy (GSMBE), usually suffer from flux intermixing[1–6] in the growth of heterointerfaces. The cross contamination of the fluxes, due to an incomplete switching or the so-called "memory effect,"[2–4] creates a compositionally graded transition layer with built-in strain, thereby deforming the shape of the well. The poorly defined well thickness generally realized by conventional growth methods makes it difficult to calculate and predict the optical properties of the resultant nonsquare potential well. Further, strain and other effects of compositional grading can result in increased nonradiative recombination at the heterointerfaces.

Improvement of heterointerface quality has been studied extensively for material systems which require a complete switch of group-V fluxes between layers, such as InGaAs/InP[1–4,6,7] and InGaP/GaAs.[5,8] Growth interruption (GI) is one of the most commonly used techniques for MOCVD,[2,7,9–11] CBE,[3,4,12] and GSMBE[5,6,13] to eliminate the formation of three-dimensional surface islands which result during the flux switching sequence. Another solution, such as introducing an evacuation time during flux switching to avoid the memory effect, has also been used. However, surface roughening is often observed by reflection high-energy electron diffraction (RHEED) when a freshly grown InP (or InGaAs) surface is exposed to $As_2$ (or $P_2$).[13,14] This roughening is believed to originate from very active P to As (or As to P) substitution. It has been proposed by Anan *et al.*[15] that the surface Ga atoms enhance the substitution of As to P based on chemical-bond-strength considerations. Recently, Vandenberg *et al.*[16] have observed interfacial strain in lattice-matched InGaAs/InP heterostructures using high resolution x-ray diffraction. A transition layer of approximately two InAsP monolayers (ML) at the InP-to-InGaAs interface was reported by Camassel *et al.*[7] A model with a 5-ML-thick quaternary transition region at the InGaAs-to-InP interface was used to explain the experimental data of Sherwin *et al.*[3] Further, Streubel *et al.*[1] have observed an approximately 230 meV redshift of the photoluminescence (PL) peak energy of a 3-ML-thick InGaAs/InP QW when the freshly grown InP surface was exposed to an As flux for roughly 12 s. Such a large shift may be due to As/P exchanges which deform the shape of the well, thus significantly affecting its optical properties. The examples mentioned above illustrate that introducing GI is not sufficient to avoid the very active exchange of As and P.

In this work, we describe a novel growth interruption sequence which results in high quality, abrupt GSMBE-grown InGaAs(P)/In(GaAs)P heterointerfaces. InGaAs(P)/In(GaAs)P MQW structures were prepared by introducing a mixed ML of In and Ga (or a ML of In)[16,17] to the surface before exposure to the new group-V flux. This mixed ML of In and Ga is shown to prevent As/P substitution. The heterointerfaces were examined by double-crystal x-ray diffraction (DCXRD) and low temperature PL. A detailed model of the resulting interface shape is consistent with the PL data, and suggests that heterointerface transition regions of only one atomic layer of InAs are achieved.

The article is organized as follows: In Sec. II we describe the switching sequences for both conventional and modified methods for the growth of the QW structures. In Sec. III, we describe the direct observation of the transition regions formed at heterointerfaces when the conventional growth sequence is used. Results of both PL spectra and DCXRD rocking curves are presented in Sec. IV, followed by the analysis and discussion of the heterointerface abruptness for both conventional and modified growth sequences. A compositionally tapered well proposed to fit the PL data of the conventional sample is also discussed. Further, simulations of DCXRD rocking curve data are presented to quantify the mismatch strain of the transition regions. In Sec. V, we present conclusions.

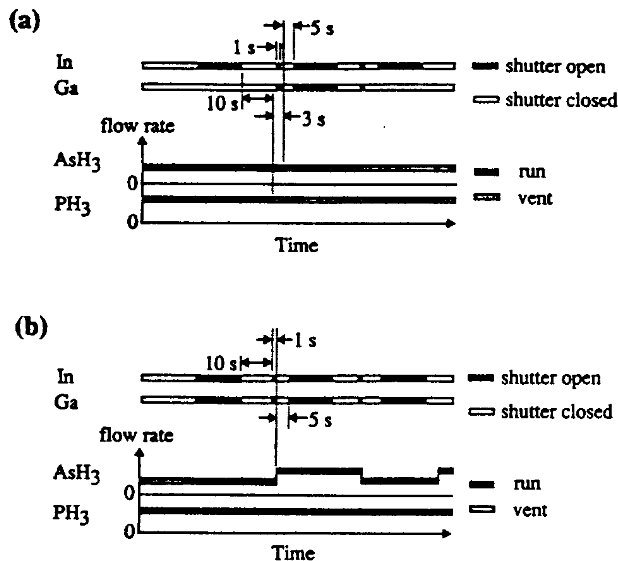


FIG. 2. Schematic schedule of the modified switching sequence for the growth of (a) $In_{0.53}Ga_{0.47}As/InP$ and (b) strained $In_{0.82}Ga_{0.18}As_{0.55}P_{0.45}/In_{0.82}Ga_{0.18}As_{0.38}P_{0.62}$ heterointerfaces.

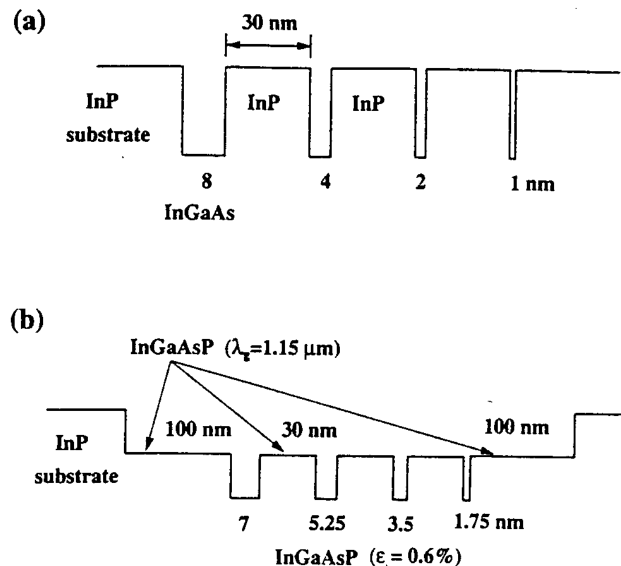


FIG. 3. Conduction band minima of (a) $In_{0.53}Ga_{0.47}As/InP$ and (b) strained $In_{0.82}Ga_{0.18}As_{0.55}P_{0.45}/In_{0.82}Ga_{0.18}As_{0.38}P_{0.62}$ MSQW structures.

surface before the new group-V gas flow was switched on. This mixed ML of In and Ga (or ML of In) was deposited to form a group-II-stabilized surface, avoiding exposure to different group-V fluxes, thereby eliminating the As/P exchange. The interfacial strain can also be reduced by this mixed ML of In and Ga since the transition layer composition is $In_{0.53}Ga_{0.47}AsP$ rather than InAsP, the latter compound having a larger lattice mismatch to InP.

### D. Multiple single quantum wells and multiple quantum well structures

Two different QW structures were prepared to study the effect of the modified GI sequence on heterointerface abruptness. The InGaAs/InP and strained $In_{0.82}Ga_{0.18}As_{0.55}P_{0.45}/In_{0.82}Ga_{0.18}As_{0.38}P_{0.62}$ multiple single quantum well (MSQW) structures were grown by both conventional and modified GI sequences (one ML In and one mixed ML of In and Ga). Here, the MSQWs [as shown in Figs. 3(a) and 3(b)] consists of four SQWs, each with a different well thickness and separated by 300-Å-thick barriers. PL at 77 K was used to characterize the sharpness of these QWs. In addition, an InGaAs/InP 20 QW structure was grown by the conventional and modified (one ML In) sequences for x-ray diffraction studies. All MQW structures have a periodicity of 180 Å, consisting of nominal well and barrier widths of 80 and 100 Å, respectively. Both 77 K PL and DCXRD were used to characterize the sharpness and the interfacial strain of the InGaAs/InP MQWs.

## III. OBSERVATION OF THE TRANSITION REGION

During growth of InGaAsP/InP double heterostructures using the conventional GI sequence described in Fig. 1(a), we observe a dramatic increase in the RHEED specular beam intensity when the P-stabilized InP surface is exposed to the mixed $As_2$ and $P_2$ fluxes [with $AsH_3/(AsH_3+PH_3)\cong 0.11$], as shown in Fig. 4. This intensity increase indicates a large change of surface coverage[19] from P to As on a P-stabilized InP surface. The RHEED pattern also indicated that the InP surface reconstruction changed from P stabilized (2×4) to As stabilized (1×2). The specular beam intensity oscillates without any group-III flux for two to three periods after switching on the $As_2$ flux. Note that intensity oscillations usually occur when the surface is exposed to a group-III flux (combined with a sufficient group-V flux), with the oscillation period corresponding to the time required for one ML growth.[20] Since there was no group-III flux introduced onto the InP surface during GI, we explain the intensity oscillations as follows. The first half-period (~0.5 s) of intensity

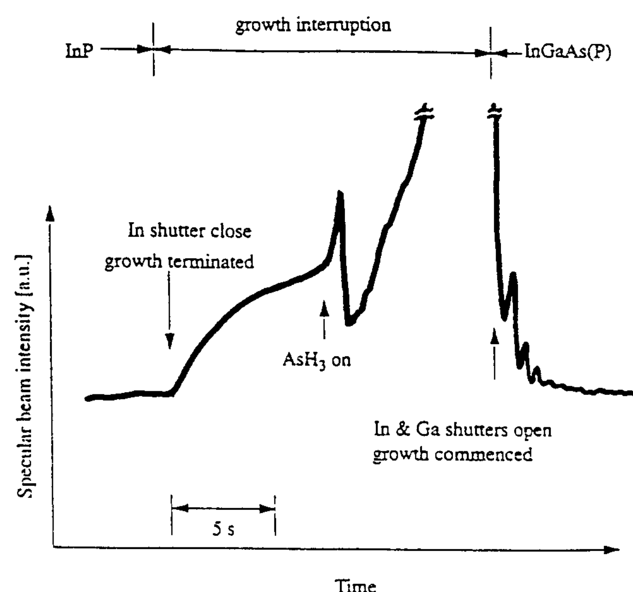


FIG. 4. Measured RHEED specular beam intensity during the growth of an InGaAsP/InP heterostructure by the conventional growth method.

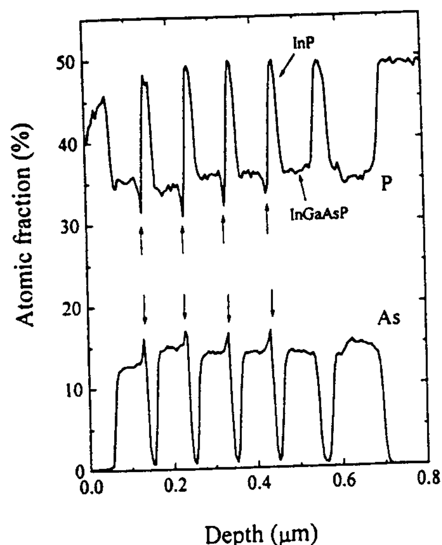


FIG. 5. A measured SIMS depth profile of an InGaAsP/InP multiple heterointerface structure.

oscillation from a maximum to a minimum (see Fig. 4) indicates a surface roughening resulting from the As/P substitution. This As/P substitution occurs very rapidly, since As or $As_2$ has a much higher sticking coefficient than P or $P_2$. The latter few intensity ripples are a result of an inward diffusion of As into the first several ML of the underlying InP layer, resulting in the As/P substitution and consequently a change of surface structure.

We also observe an abrupt decrease of P and an increase of As at the InGaAsP-to-InP interface in the secondary ion mass spectroscopy (SIMS) composition profile (see Fig. 5). The SIMS measurement was performed by Cs bombardment and by detecting the $CsX^+$ cluster ion, which has been reported by Magee *et al.*[21] to have nearly equal sensitivity for all four matrix elements of InGaAsP. The P and As spikes at each heterointerface indicate an abrupt change in the surface coverage of P, consistent with the RHEED data. Once the surface composition changes, it affects the composition of the subsequent layer, forming a strained transition region. The SIMS data shown that, in contrast to the "memory effect," this transition layer is rich in As. From Fig. 5, we note that the P-to-As substitution is not as pronounced at the InGaAsP-to-InP interface when compared to the As-to-P substitution at the InP-to-InGaAsP interface. This reveals that not only do surface Ga atoms enhance the P-to-As substitution as proposed by Anan *et al.*,[15] but also surface In atoms actively enhance the As-to-P substitution. From this we infer that the As/P exchange occurs more readily at $In_{0.53}Ga_{0.47}As$-to-InP interfaces since a complete group-V switching is required.

## IV. RESULTS AND DISCUSSION

### A. PL of heterointerfaces

PL spectra measured at 77 K for InGaAs/InP and strained InGaAsP/InGaAsP MSQW structures grown by conventional and modified GI sequences are shown in Figs. 6(a)

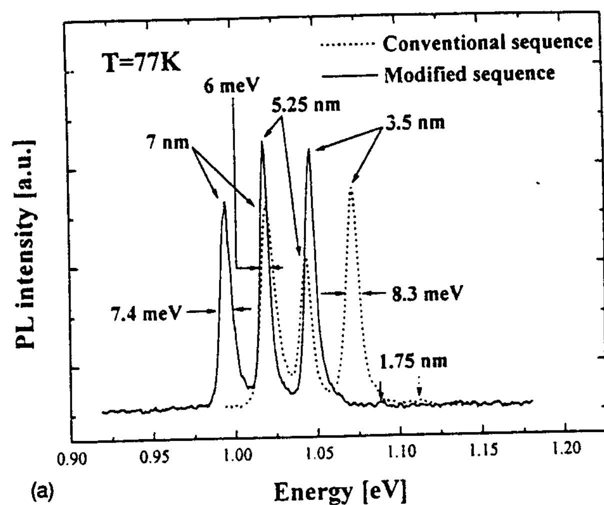


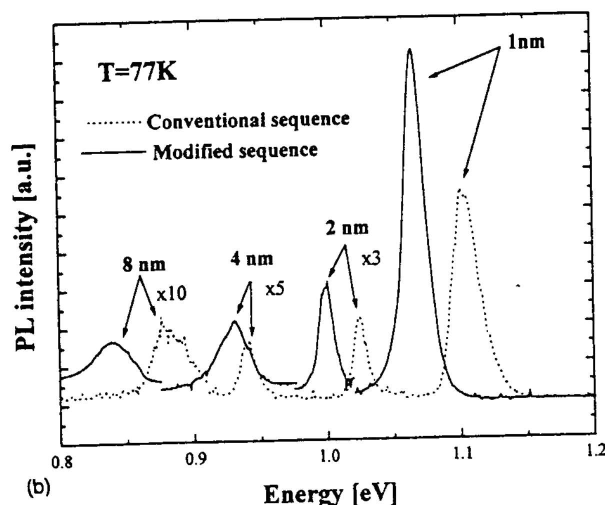


FIG. 6. 77 K PL spectra of (a) strained $In_{0.82}Ga_{0.18}As_{0.55}P_{0.45}$/$In_{0.82}Ga_{0.18}As_{0.38}P_{0.62}$ and (b) $In_{0.53}Ga_{0.47}As$/InP MSQW grown by conventional (dashed) and modified (solid) sequences.

and 6(b), respectively. Two important features are revealed in these spectra. First, all PL peaks for samples grown by modified GI sequences are shifted to a lower energy relative to the conventionally grown samples. Second, the PL peak energies are more equally spaced for samples grown by conventional means, indicating an approximately parabolic potential well shape.

In order to characterize the well shape, the PL peak energies versus well width are plotted as points in Figs. 7(a) and 7(b). Calculated curves based on a square-well approximation with a conduction band offset of $\Delta E_c=0.39\Delta E_g$ for unstrained InGaAsP/InP,[22] and $\Delta E_c=0.5\Delta E_g$ for strained InGaAsP/InGaAsP[23–25] heterojunctions are also shown as solid lines in Fig. 7. Here, $\Delta E_g$ is the band-gap discontinuity at the heterojunction. For both modified sequence-grown MSQW samples, the PL data agree with the square-well approximation, indicating QWs with a nearly perfect square-well shape were obtained. On the other hand, the PL data for the conventional sequence-grown samples cannot be fit by the square-well approximation, especially for the InGaAs/InP sample whose PL data are redshifted for narrow wells (10 Å), and blue shifted for wider wells (20, 40, and 80 Å) when

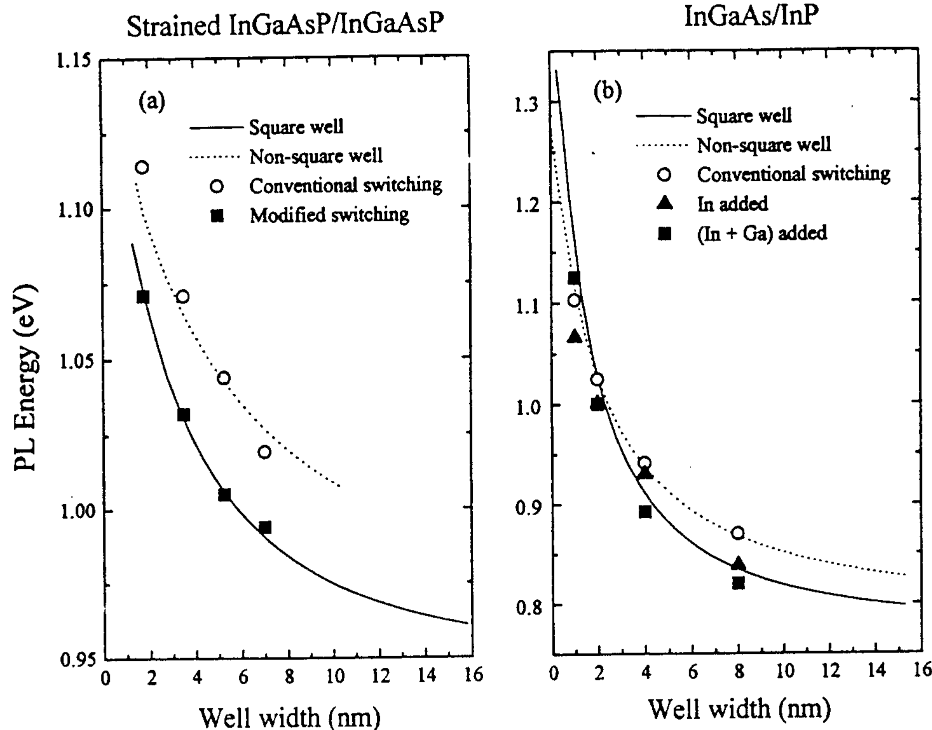


FIG. 7. PL peak energies vs QW width of the (a) strained $In_{0.82}Ga_{0.18}As_{0.55}P_{0.45}/In_{0.82}Ga_{0.18}As_{0.38}P_{0.62}$ and (b) $In_{0.53}Ga_{0.47}As/InP$ MSQWs. Solid lines are for the square-well approximation. Dashed lines are the best fit obtained using a nonsquare potential profile as described in Fig. 8(a).

compared to the calculated square-well curve.

A compositionally tapered potential well resulting from species interdiffusion at the heterointerfaces is proposed [Fig. 8(a)] to explain the dependence of luminescence energy on well width observed in Fig. 7. In this non-square-well approximation, graded regions A and C are formed by the As/P exchange (inferred from RHEED data), while B and D are due to an incomplete group-V switching (suggested by the SIMS results). Note that graded region B is many tens of angstroms thick, consistent with the SIMS data. The effect of graded regions A and D is to lower the electron energy level, while B and C lead to an increase in energy. For a nonsquare narrow well as shown in Fig. 8(b), the electron level (which is high in the well) shifts to a lower energy compared to the same level in a square well. In contrast, for a wide tapered well shown in Fig. 8(c), the low-lying electron level shifts to a higher energy compared to a square well with the same width since the effect from graded regions B and C dominates in this case. The observed, slow decrease in PL energy with increasing well width compared to the square well is then expected. The solution to Schrödinger's equation for this nonsquare potential well with parabolic region B has been used to fit the conventional GI sequence data. The composition of the surface $InAs_yP_{1-y}$ layer and the linearly tapered region width, $d$ [as defined in Fig. 8(a)] were used as fitting parameters. The best fit [shown in Fig. 7(b) as a dashed line] obtained for InGaAs/InP QWs shows that the interface layer composition is $InAs_{0.7}P_{0.3}$ grown by conventional sequences, indicating a surface coverage change from 100% P to 30% P+70% As. Also, a graded ~4-ML-thick transition layer of $InAs_yP_{1-y}$ has been formed at the InP-to-InGaAs interface. For the InGaAs-to-InP interface, however, no transition layer was used for the fit since P/As substitution is not as active as the As/P substitution at the InP-to-InGaAs interface, as determined by SIMS measurements.

For strained InGaAsP/InGaAsP MSQWs, the curve fitting is complicated by the fact that strain induces changes of material parameters[26] such as the valence band effective mass, band gap, and conduction and valence band offsets. In fitting the experimental data, we have introduced the strain-induced material parameters except for the hole effective

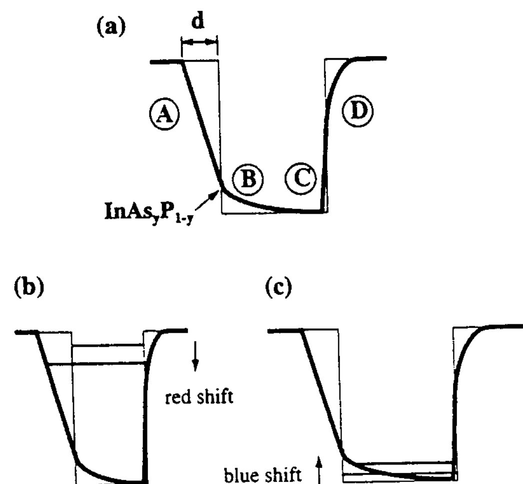


FIG. 8. (a) A proposed nonsquare well for the conventional growth sequence. Graded regions A and C are formed by As/P exchange, while B and D are due to an incomplete group-V switching. (b) Schematic illustration of the redshift of the electron level in a "narrow" well and (c) the blueshift of the electron level of a "wide" well.

TABLE I. Summary of the experimental data and the parameters used in the DCXRD simulations.

| | Experiment ($C$)[a] | Simulation ($C$) | Experiment ($M$) | Simulation ($M$) | Simulation ($S$) |
|---|---|---|---|---|---|
| $\Lambda_{QW}$ (Å) | 180 | 180 | 180 | 180 | 180 |
| $t_B$ (Å)[b] | 100 | 88 | 100 | 98.5 | 100 |
| $t_{B\rightarrow W}$ (Å) | | 12 | | 1.5 | 0 |
| $t_W$ (Å) | 80 | 80 | 80 | 78.5 | 80 |
| $t_{W\rightarrow B}$ (Å) | | 0 | | 1.5 | 0 |
| $\epsilon_{B\perp}$ [c] | | 0 | | 0 | 0 |
| $\epsilon_{B\rightarrow W\perp}$ | | Graded from 0 to +2% ($InAs_{0.7}P_{0.3}$) | | Graded from +3.1% (InAs) to $-1\times10^{-3}$ (InGaAs) | 0 |
| $\epsilon_{W\perp}$ [d] | | Graded from −1.6% ($In_{0.53}Ga_{0.47}As_{0.7}P_{0.3}$) to $-1\times10^{-3}$ ($In_{0.53}Ga_{0.47}As$) | | $-1\times10^{-3}$ | $-1\times10^{-3}$ |
| $\epsilon_{W\rightarrow B\perp}$ | | 0 | | graded from $-1\times10^{-3}$ (InGaAs) to +3.1% (InAs) | 0 |
| $\epsilon_{QW\perp}$ | $-1.1\times10^{-3}$ | $-1.2\times10^{-3}$ | $-6\times10^{-4}$ | $-4\times10^{-4}$ | $-4.4\times10^{-4}$ |
| $\delta\omega_0$ [e] (arcsec) | $+140\pm30$ | +150 | $+75\pm30$ | +50 | +56 |

[a] $C$, $M$, and $S$ represent conventional switching, modified switching, and ideal square well, respectively.
[b] $t_i$ is the total thickness $t_i=d_iN_i$, where $d_i$ is the atomic spacing along [100]. Also, $d_i$'s and $N_i$'s are the atomic spacing and number of diffracting planes of layer $i$: barrier ($B$), barrier-to-well ($B\rightarrow W$), well ($W$), and well-to-barrier ($W\rightarrow B$) layers.
[c] $\epsilon_{i\perp}$ is the strain along [100] of layer $i$, while $\epsilon_{QW\perp}$ is the average strain along [100] of the QWs.
[d] $\epsilon_{w\perp}$ is obtained by assuming a Poisson ratio of 0.5 and a lattice mismatch of $-5\times10^{-4}$ for InGaAs well. A compositional graded $In_{0.53}Ga_{0.47}As_yP_{1-y}$ well with an $\epsilon_{W\perp}$ profile same as region $B$ in Fig. 8(a) is used for the simulation of the conventional growth method.
[e] $\delta\omega_0$ is the angular separation between the $m=0$ satellite peak and the InP substrate peak.

separation between the $m=0$ and the substrate peaks for the simulated and experimental data is shown in Fig. 10(a), thereby confirming the presence of strained transition regions at the conventionally grown heterointerfaces. On the other hand, an x-ray simulation using the atomic-composition profile described by (iii) above, with only one atomic layer of InAs at both heterointerfaces has been done to compare with the x-ray data of the modified sequence. A match of the zeroth-order peak position for the simulated and experimental data is shown in Fig. 10(b). This match is extremely sensitive to fitting parameters such as the thickness and composition of the transition layer. If the transition layer is graded from the first atomic layer, which is InAs as proposed by atomic profile (iii), to the well layer, which is $In_{0.53}Ga_{0.47}As$, then the fitting shown in Fig. 10(b) becomes unique. The excellent match of the data to the profile (iii) therefore is an additional indication that a square well with ML abruptness was grown by the modified GI sequence. Comparing Figs. 10(a) and 10(b), we find that the satellite peak intensities are enhanced by the presence of strain,[32,33] consistent with the simulation results.

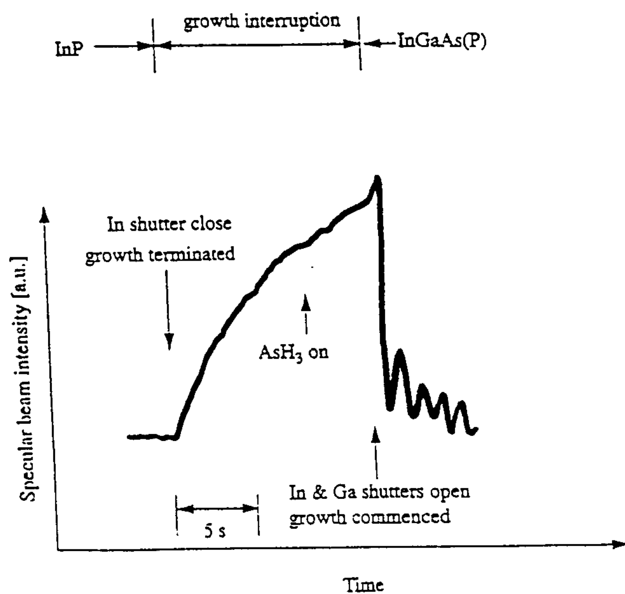


FIG. 11. Measured RHEED specular beam intensity during the growth of an InGaAsP/InP heterostructure by the modified growth method.

Finally, the RHEED specular beam intensity oscillations recorded during the modified growth method of InGaAsP/InP heterostructures are shown in Fig. 11. Comparing these data to Fig. 4, we find that the dramatic fluctuation in the RHEED intensity, which occurs when introducing the new group-V flux during the conventional growth method, no longer appears in Fig. 11. This indicates a reduced As/P substitution, thereby a more abrupt heterointerface.

## V. CONCLUSION

We have demonstrated a novel group-V switching sequence for the gas source molecular beam epitaxial growth of InGaAs(P)/In(GaAs)P MQW structures which results in improved interface abruptness. Growth of high quality InGaAs(P)/In(GaAs)P MQW structures was demonstrated by introducing a mixed monolayer of In and Ga to the surface before the exposure of the surface to the new group-V flux. Heterointerfaces were characterized by both DCXRD and PL. The results show that both DCXRD and PL data fit a square well with monolayer heterointerface abruptness for the modified growth method, while the data fit a graded in-

terface nonsquare well model when conventional switching sequences are used. These results suggest that interfaces grown by the modified sequences should result in improved heterointerface and MQW device quality.


## ACKNOWLEDGMENTS

The authors would like to thank Dr. Magee for his help in the SIMS analysis. The authors also acknowledge RADC/ARPA (J. Lorenzo and R. Leheny), AFOSR (A. Craig), ONR (Y. S. Park), and the National Science Foundation for their support of this work.



[1] K. Streubel, F. Scholz, and V. Härle, *Proceedings of the Third International Conference on InP and Related Materials*, edited by T. Riley (IEEE, New York, 1991), p. 468.

[2] T. Y. Wang, E. H. Reihlen, H. R. Jen, and G. B. Stringfellow, J. Appl. Phys. **66**, 5376 (1989).

[3] M. E. Sherwin, F. L. Terry, Jr., G. O. Munns, J. S. Herman, E. G. Woelk, and G. I. Haddad, J. Electron. Mater. **21**, 269 (1992).

[4] A. Antolini, P. J. Bradley, C. Cacciatore, D. Campi, L. Gastaldi, F. Genova, M. Iori, C. Lamberti, C. Papuzza, and C. Rigo, J. Electron. Mater. **21**, 233 (1992).

[5] H. Y. Lee, M. J. Hafich, G. Y. Robinson, K. Mahalingam, and N. Otsuka, J. Cryst. Growth **111**, 525 (1991).

[6] B. Elman, E. S. Koteles, D. Kenneson, J. Powers, and D. Oblas, *Proceedings of the Fourth International Conference on InP and Related Materials* (IEEE, New York, 1992), p. 175.

[7] J. Camassel, J. P. Laurenti, S. Juillaguet, F. Reinhardt, K. Wolter, H. Kurz, and D. Grützmacher, J. Cryst. Growth **107**, 543 (1991).

[8] H. Y. Lee, M. J. Hafich, and G. Y. Robinson, J. Cryst. Growth **105**, 244 (1990).

[9] J. Hergeth, D. Grützmacher, F. Reinhardt, and P. Balk, J. Cryst. Growth **107**, 537 (1991).

[10] G. Landgren, J. Wallin, and S. Pellegrino, J. Electron. Mater. **21**, 105 (1992).

[11] G. Landgren, P. Ojala, and O. Ekström, J. Cryst. Growth **107**, 573 (1991).

[12] A. Antolini, L. Francesio, L. Gastaldi, F. Genova, C. Lamberti, L. Lazzarini, C. Papuzza, C. Rigo, and G. Salviati, J. Cryst. Growth **127**, 189 (1993).

[13] K. Mahalingam, Y. Nakamura, N. Otsuka, H. Y. Lee, M. J. Hafich, and G. Y. Robinson, J. Electron Mater. **21**, 129 (1992).

[14] J. F. Carlin, R. Houdré, A. Rudra, and M. Ilegems, Appl. Phys. Lett. **59**, 3018 (1991).

[15] T. Anan, S. Sugou, K. Nishi, and T. Ichihashi, Appl. Phys. Lett. **63**, 1047 (1993).

[16] J. M. Vandenberg, A. T. Macrander, R. A. Hamm, and M. B. Panish, Phys. Rev. B **44**, 3991 (1991).

[17] J. M. Vandenberg, M. B. Panish, R. A. Hamm, and H. Temkin, Appl. Phys. Lett. **56**, 910 (1990).

[18] RIBER Div., Instruments SA, Inc., Edison, NJ.

[19] Arsenic has a higher atomic scattering factor ($f$) than phosphorus: *International Tables for X-ray Crystallography*, edited by K. Lonsdale (Kynoch, Birmingham, 1968), Vol. III.

[20] J. H. Neave, B. A. Joyce, P. J. Dobson, and N. Norton, Appl. Phys. A **31**, 1 (1983).

[21] C. W. Magee, W. L. Harrington, and E. M. Botnick, Int. J. Mass Spectrom. **103**, 45 (1990).

[22] S. R. Forrest, P. H. Schmidt, R. B. Wilson, and M. L. Kaplan, Appl. Phys. Lett. **45**, 1199 (1984).

[23] D. Gershoni, J. M. Vandenberg, R. A. Hamm, H. Temkin, and M. B. Panish, Phys. Rev. B **36**, 1320 (1987).

[24] R. E. Cavicchi, D. V. Lang, D. Gershoni, A. M. Sergent, J. M. Vandenberg, S. N. G. Chu, and M. B. Panish, Appl. Phys. Lett. **54**, 739 (1989).

[25] C. Stark, J.-Y. Emery, R. J. Simes, M. Matabon, L. Goldstein, and J. Barrau, J. Cryst. Growth **120**, 180 (1992).

[26] J. P. Loehr and J. Singh, IEEE J. Quantum Electron. **27**, 708 (1991).

[27] Note that $e^{-\Delta E/kT}=0.5 \Rightarrow \Delta E=0.7kT$.

[28] V. Sperious and T. Vreeland, Jr., J. Appl. Phys. **56**, 1591 (1984).

[29] J. M. Vandenberg, R. A. Hamm, M. B. Panish, and H. Temkin, J. Appl. Phys. **62**, 1278 (1987).

[30] J. M. Vandenberg, M. B. Panish, H. Temkin, and R. A. Hamm, Appl. Phys. Lett. **53**, 1920 (1988).

[31] S. T. Picraux, B. L. Doyle, and J. Y. Tsao, in *Semiconductors and Semimetals*, edited by R. K. Willardson and A. C. Beer (Academic, San Diego, 1991), Vol. 33, Chap. 3.

[32] W. J. Bartels, J. Vac. Sci. Technol. B **1**, 338 (1983).

[33] M. H. Lyons, J. Cryst. Growth **96**, 339 (1989).

# Low-Threshold, High-Power, 1.3-$\mu$m Wavelength, InGaAsP–InP Etched-Facet Folded-Cavity Surface-Emitting Lasers

C.-P. Chao, D. Z. Garbuzov, G.-J. Shiau, S. R. Forrest, *Fellow, IEEE*, L. A. DiMarco, and M. G. Harvey

***Abstract*—A 1.3-$\mu$m wavelength, InGaAsP–InP folded-cavity, surface-emitting laser with $CH_4$–$H_2$ reactive ion-etched vertical and 45° angled facets was demonstrated for the first time. Continuous-wave threshold currents of 32 mA have been achieved, with >15 mW CW power for the surface-emitted light. These surface-emitting lasers with two dry-etched facets are suitable for wafer-level testing and for monolithic integration with other InP-based photonic devices.**

LONG-WAVELENGTH InP–InGaAsP surface-emitting lasers (SEL's) are useful for optical communications and two-dimensional optoelectronic interconnections employing InP-based optoelectronic integrated circuits [1]. Research on 1.3-$\mu$m and 1.55-$\mu$m-long wavelength SEL's has been centered on four different types of laser structures: vertical-cavity SEL's [2]–[3], grating SEL's [4], integrated-deflector SEL's (IDSEL's) [5]–[6], and folded-cavity SEL's (FCSEL's) [7]–[9]. To date, some of the most successful SEL's utilize high temperature (740 °C) mass transported integrated deflectors [5], or wafer-fused GaAs–AlAs vertical-cavity mirrors [2]. Unfortunately, the high temperature processes and/or complicated structures of these devices are not readily compatible with monolithic integration of devices such as transistors and detectors.

In this respect, FCSEL's and IDSEL's with etched beam-deflectors for surface-emission, and a simple p-i-n material structure with a fabrication process nearly identical to that of simple etched-facet lasers, can be easily incorporated into InP photonic integrated circuits. Considerable work on etched-facet InP IDSEL's has recently been reported with threshold currents of approximately 30 mA [6]. Unfortunately, most devices of this type suffer from low output efficiency. On the other hand, compared to an external deflector, the 45° total internal reflection mirror of a FCSEL exhibits superior deflecting efficiency, and requires no high-reflectivity coatings, and high performance FCSEL's based on GaAs material have already been demonstrated [10]. For InP–InGaAsP FCSEL's, many technologies, such as inclined reactive ion beam etching [6] and focused ion beam etching [8] have been adopted for the formation of the 45° facet, and devices reported to date still exploit one cleaved facet primarily due to the inferior quality of the etched 45° mirror.

Following the demonstration of a precisely etched InP–InGaAsP 45° facet [9], in this work we report the fabrication of 1.3-$\mu$m wavelength, strained MQW InP–InGaAsP FCSEL's with 45° angle and vertical facets. With both facets dry-etched, these devices can be tested at the wafer level, and can be readily integrated with other long-wavelength optoelectronic devices. A low, continuous-wave (CW) threshold current of 32 mA and 18% efficiency for the surface-emitted light was achieved for 4-$\mu$m-wide by 600-$\mu$m-long devices. Threshold current as low as 25 mA was measured for 470-$\mu$m-long devices with one facet cleaved. To our knowledge, this is the first demonstration of truly integratable InP–InGaAsP FCSEL's, and the threshold current represents a 30% improvement over the lowest value reported to date for 1.3 $\mu$m wavelength FCSEL's [9]. Furthermore, a CW power >15 mW for vertical light emission is observed, which is comparable to the best value reported to date for SEL's at this wavelength [6].

The laser wafer was grown by gas-source molecular beam epitaxy (GSMBE) on a S-doped $n^+$ InP substrate. A 1-$\mu$m thick, lightly Si-doped ($2 \times 10^{17}$ cm$^{-3}$) InP lower cladding layer was first grown, followed by a 1200-Å thick, undoped InGaAsP lower waveguide layer which had a bandgap cutoff wavelength of $\lambda_g = 1.15$ $\mu$m. After growth of the undoped active region, a 1200-Å-thick, InGaAsP $\lambda_g = 1.15$ $\mu$m upper waveguide layer was grown. The active region consists of five compressively strained InGaAsP quantum wells with 105-Å wide barriers ($\lambda_g = 1.15$ $\mu$m) and 67-Å wide wells ($\lambda_g = 1.4$ $\mu$m). Finally, we grew a 1.2-$\mu$m thick, Be-doped ($2 \times 10^{17}$ cm$^{-3}$ to $5 \times 10^{17}$ cm$^{-3}$) InP upper cladding layer, and an 800-Å-thick, $p^+$ InGaAs top contact layer Be-doped to $\sim 2 \times 10^{18}$ cm$^{-3}$.

The device, shown schematically in Fig. 1, exploits a 45° facet, a vertical facet, and a ridge waveguide, all formed by dry etching using a $CH_4$–$H_2$ plasma. The device processing started by patterning 4-$\mu$m-wide by 600-$\mu$m-long $SiN_x$ (2000-Å thick) strips that served as a dry-etching mask for the ridge waveguide. The ridge etching was stopped ~2000 Å above the undoped waveguide region. A flat surface

Manuscript received January 30, 1995; revised April 7, 1995. This work was supported in part by Rome Labs/ARPA, AFOSR, and US Army/CECOM.

C.-P. Chao, D. G. Garbuzov, and S. R. Forrest are with the Advanced Technology Center for Photonics and Optoelectronic Materials, Department of Electrical Engineering, Princeton University, Princeton, NJ 08544 USA.

G.-J. Shiau was with the Advanced Technology Center for Photonics and Optoelectronic Materials, Department of Electrical Engineering, Princeton University, Princeton, NJ 08544 USA; he is now with Applied Materials, Inc., San Jose, CA 95054 USA.

L. A. DiMarco and M. G. Harvey are with the David Sarnoff Research Center, Princeton, NJ 08540 USA.

IEEE Log Number 9412716.

1041-1135/95$04.00 © 1995 IEEE

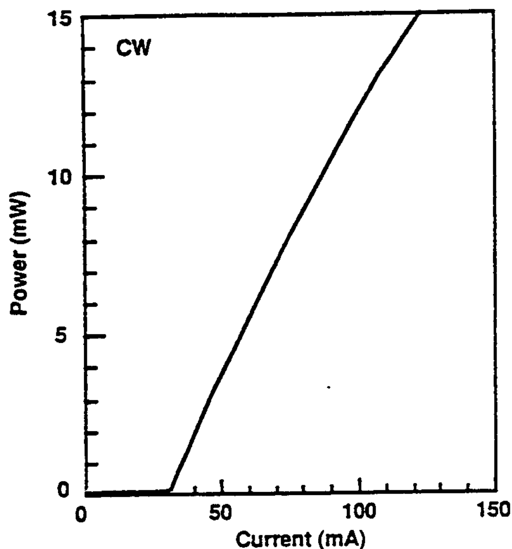


Fig. 3. CW light-current characteristics of a 600-$\mu$m-long by 4-$\mu$m-wide etched-facet FCSEL.

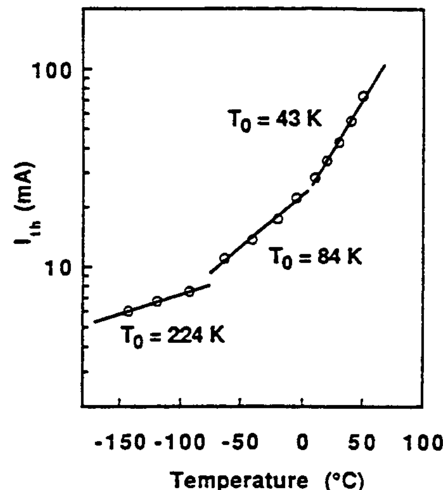


Fig. 4. CW threshold current versus temperature for a FCSEL with two etched facets. The different characteristic temperatures ($T_0$) over different temperature ranges are indicated.

spectrum becomes multimode. The single-mode operation of this device is quite different from the published data reported for cleaved-facet laser diodes. Preliminary study indicates that the multiple reflections from the two etched facets and the step at the end of the ridge waveguide (in effect, forming a coupled cavity structure) might contribute to the high side-mode suppression in this device. However, further investigation of this important difference between InP-based FCSEL's and cleaved-facet lasers is currently underway.

The CW $I_{th}$ measured as a function of temperature from $-143$ °C–50 °C is shown in Fig. 4. The characteristic temperature ($T_0$) is 224 K for $T < -90$ °C, 84 K for $T < 0$°C, and 43 K for $T > 0$°C. The low temperature $T_0$ is comparable to that obtained for conventional, 1.3-$\mu$m wavelength MQW InP–InGaAsP lasers, whereas the $T_0$ around room temperature is only about half that of the cleaved-facet laser (where $T_0 \sim 80$ K–100 K). This is primarily due to the n-side down bonding and the relatively high contact resistance ($\sim$13 $\Omega$) of our FCSEL's.

In conclusion, we have fabricated GSMBE-grown, 1.3-$\mu$m wavelength, strained MQW InP–InGaAsP etched-facet FCSEL's with a very low CW threshold current of 32 mA. To our knowledge, this is the first demonstration of high-performance, etched-facet, 1.3-$\mu$m FCSEL's. With wafer-level bonding on a heat sink, a surface-normal power in excess of 15 mW was achieved. Single longitudinal-mode operation with >15 dB side-mode suppression was observed. The simple and reproducible high-quality etching of the 45° and vertical facets in a conventional $CH_4$–$H_2$ RIE system made these FCSEL's attractive for applications that require monolithic integrated lasers with other InP-based optoelectronic devices.

## Acknowledgment

The authors thank M. J. Lange for his help in this work.

## References


[1] S. Yu and S. R. Forrest, "Implementations of smart pixels for optoelectronic processors and interconnection," *J. Lightwave Technol.*, vol. 11, pp. 1659–1669, 1993.

[2] J. J. Dudley, D. I. Babic, R. Mirin, L. Yang, B. I. Miller, R. J. Ram, T. Reynolds, E. L. Hu, and J. E. Bowers, "Low threshold, wafer fused long wavelength vertical cavity lasers," *Appl. Phys. Lett.*, vol. 64, pp. 1463–1465, 1994.

[3] D. I. Babic, J. J. Dudley, K. Streubel, R. P. Mirin, N. M. Margalit, J. E. Bowers, and E. L. Hu, "Double-fused 1.52 $\mu$m vertical-cavity lasers," *IEEE LEOS '94*, paper PD1.4, Boston, MA, Nov. 1994.

[4] C. Wu, M. Svilans, M. Fallahi, T. Makino, J. Glinski, C. Maritan, and C. Blaauw, "Optically pumped surface-emitting DFB GaInAsP/InP lasers with circular grating," *Electron. Lett.*, vol. 27, pp. 1819–1820, 1991.

[5] Z. L. Liau and J. N. Walpole, "Surface-emitting GaInAsP/InP laser with low threshold current and high efficiency," *Appl. Phys. Lett.*, vol. 46, pp. 115–117, 1985.

[6] H. Saito and Y. Noguchi, "A reflection-type surface-emitting 1.3 $\mu$m InGaAsP/InP laser array with microcoated reflector," *Jpn. J. Appl. Phys. Lett.*, vol. 28, pp. L1239–L1241, 1989.

[7] B. Stegmüller, H. Westermerier, W. Thulke, G. Franz, and D. Sacher, "Surface emitting InGaAsP/InP distributed feedback laser diode at 1.53 $\mu$m with monolithic integrated microlens," *Photon. Technol. Lett.*, vol. 3, pp. 776–778, 1991.

[8] H. P. Lee, A. Scherer, E. D. Beebe, W. P. Hong, R. Bhat, and A. A. Koza, "1.57 $\mu$m InGaAsP/InP surface emitting lasers by angled focus ion beam etching," *Electron. Lett.*, vol. 28, pp. 580–581, 1991.

[9] C.-P. Chao, G.-J. Shiau, and S. R. Forrest, "1.3 $\mu$m wavelength, InGaAsP/InP folded-cavity surface-emitting grown by gas source molecular beam epitaxy," *Photon. Technol. Lett.*, vol. 6, pp. 1406–1408, 1994.

[10] W. D. Goodhue, J. P. Donnelly, C. A. Wang, G. A. Lincoln, K. Rauschenbach, R. J. Bailey, and G. D. Johnson, "Monolithic two-dimensional surface-emitting strained-layer InGaAs/AlGaAs and AlInGaAs/AlGaAs diode laser arrays with over 50% differential quantum efficiencies," *Appl. Phys. Lett.*, vol. 59, pp. 632–634, 1991.

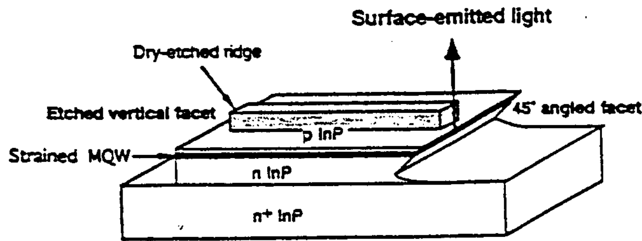


Fig. 1. Schematic diagram of a GaInAsP–InP etched-facet FCSEL with dry-etched vertical and 45° facets.

was preserved on both ends of the ridge waveguide for the facet etchings. A 6000-Å thick $SiN_x$ layer was deposited for p-contact isolation. The $SiN_x$ on top of the ridge was removed by a photoresist planarization process, followed by depositing a 50-μm wide, Ti–Pt–Au (200 Å/500 Å/4000 Å) p-contact pad. All three dry-etching processes (i.e., the two facets and ridge guide) were carried out in a conventional reactive ion etching system using a 1:5 $CH_4$–$H_2$ mixture at 30 mtorr. The self-bias was 500 V for the ridge etching, and was raised to 660 V for the vertical and 45° facet etchings to enhance the directionality of the ions. To remove polymer accumulation during etching, a 2-min $O_2$ plasma back-etch was applied periodically after every 5 min of $CH_4$–$H_2$ etching. A custom-designed laser wafer holder reported previously [9] was used for the 45° facet formation. The etch rate was ~500 Å/min for the normal facet, and ~360 Å/min along the angled facet. Smooth and highly directional etching of the vertical and undercut 45° facets was observed. After a slight polishing, we deposited Ge–Au–Ni–Au (270 Å/450 Å/215 Å/1200 Å) on the substrate side for the n-contact metal, followed by a 90-s, 365 °C rapid thermal contact anneal to complete the process.

The devices were tested at the wafer level under pulsed operation (1 μs, 10 kHz) without a heat sink. Shown in Fig. 2 are the room-temperature light-current (L–I) characteristics for a 4-μm wide by 600-μm long etched-facet FCSEL, and for a 4-μm-wide by 470-μm-long FCSEL with one facet cleaved. Also shown in the figure is the emission spectrum of the etched-facet FCSEL at $I = 45$ mA, where we observe a wavelength of 1.32 μm, and a 15 dB side-mode suppression. The threshold current ($I_{th}$) and the quantum efficiency ($\eta_s$) for the surface-emitted light are 32 mA and 18% for the etched-facet FCSEL, and 25 mA and 25% for the cleaved-facet FCSEL, respectively. Both device results represent a substantial reduction in the threshold current for long-wavelength FCSEL's, and the efficiencies are also among the highest reported to date for any InP–InGaAsP long-wavelength SEL's, second only to the IDSEL made using mass transport [5].

To more accurately determine the quality of the etched facets, we measured the L–I characteristics for 460-μm long, conventional cleaved-facet lasers, and 560-μm long cleaved-facet FCSEL's with the same ridge width. The cleaved-facet lasers have a threshold current of from $I_{th} = 22$ to 24 mA, with 24% quantum efficiency per facet, and the 560-μm long FCSEL's have $I_{th} = 30$ mA with $\eta_s = 20\%$ (15% for edge-emitted light, $\eta_e$). The higher surface-emitting quantum efficiency is due to the smaller reflectivity for the 45° mirror as opposed to the cleaved facet. The comparable $I_{th}$ and

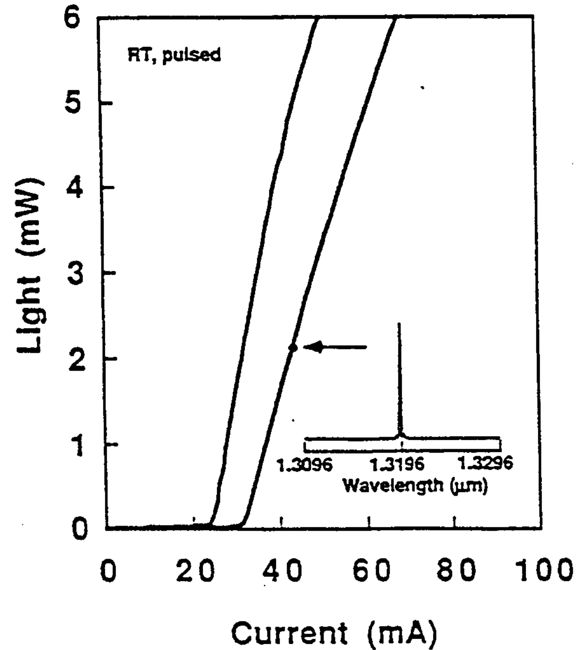


Fig. 2. Surface-emitted light-current characteristics for lasers under pulsed operation for (a) a 600-μm by 4-μm etched-facet FCSEL (the emission spectrum at 45 mA is also shown) and (b) a 470-μm by 4-μm FCSEL with one cleaved facet.

efficiency for devices of similar length indicated that the performance degradation due to the etched facets was minimal. Following the method suggested in [9], and using an internal loss $\alpha_i = 10$ cm$^{-1}$, internal efficiency $\eta_i = 60\%$, (both values typical for 4-μm wide ridge lasers grown in our laboratory), and $\eta_s$ and $\eta_e$ as mentioned above, the reflectivity of the 45° facet ($R_s$) for the 560-μm cleaved-facet FCSEL was estimated to be 20%, with an additional 15% loss ($S_s$) primarily due to diffraction in the unguided cavity portion. Assuming the same $R_s$ and $S_s$ for the etched-facet FCSEL's, the reflectivity at the etched vertical facet ($R_e$) can be estimated from the following equation:

$$\eta_s = \eta_i \frac{\alpha_m}{\alpha_m + \alpha_i} \frac{1}{1+\chi} \frac{1-R_s-S_s}{1-R_s}$$

where $L = 600$ μm is the device length, and

$$\chi = \frac{1-R_e}{1-R_s}\sqrt{\frac{R_s}{R_e}}, \quad \text{and} \quad \alpha_m = \frac{1}{2L}\ln\left(\frac{1}{R_s R_e}\right).$$

The only unknown variable, $R_e$, was calculated to be 22%, which is 10% less than for a cleaved facet. This difference was larger than expected for a high-quality dry-etched vertical facet, and might have been caused by multiple reflections between the etched facet and the ridge end, since the ridge was terminated ~3–5 μm before reaching the facet.

Fig. 3 is the CW L–I characteristic for a 600-μm long etched-facet FCSEL bonded n-side down on a Cu heat sink. For this device, we find that $I_{th} = 32$ mA and $\eta_d = 18\%$, and a high-output power of 15 mW. The emission spectrum measurement exhibited a dominant lasing mode at $\lambda = 1.3206$ μm, and a 13-dB side-mode suppression was observed around $I = 86$ mA. For currents >100 mA, the

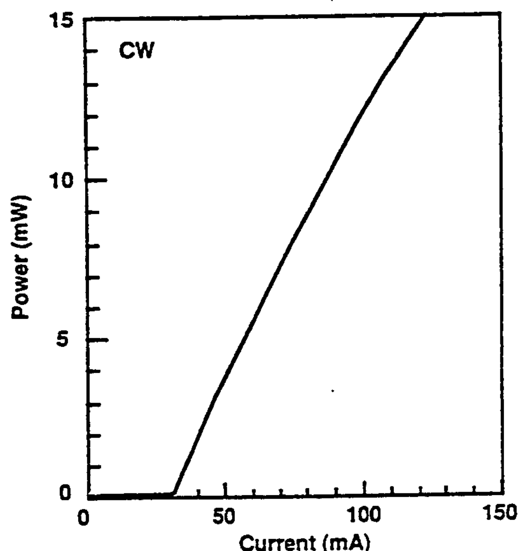


Fig. 3. CW light-current characteristics of a 600-$\mu$m-long by 4-$\mu$m-wide etched-facet FCSEL.

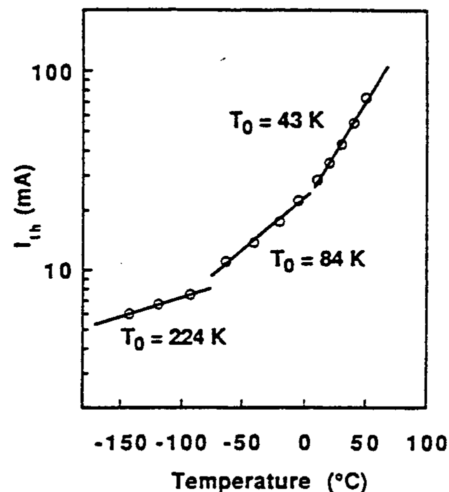


Fig. 4. CW threshold current versus temperature for a FCSEL with two etched facets. The different characteristic temperatures ($T_0$) over different temperature ranges are indicated.

spectrum becomes multimode. The single-mode operation of this device is quite different from the published data reported for cleaved-facet laser diodes. Preliminary study indicates that the multiple reflections from the two etched facets and the step at the end of the ridge waveguide (in effect, forming a coupled cavity structure) might contribute to the high side-mode suppression in this device. However, further investigation of this important difference between InP-based FCSEL's and cleaved-facet lasers is currently underway.

The CW $I_{th}$ measured as a function of temperature from $-143$ °C–50 °C is shown in Fig. 4. The characteristic temperature ($T_0$) is 224 K for $T < -90$ °C, 84 K for $T < 0$°C, and 43 K for $T > 0$°C. The low temperature $T_0$ is comparable to that obtained for conventional, 1.3-$\mu$m wavelength MQW InP–InGaAsP lasers, whereas the $T_0$ around room temperature is only about half that of the cleaved-facet laser (where $T_0 \sim 80$ K–100 K). This is primarily due to the n-side down bonding and the relatively high contact resistance ($\sim$13 $\Omega$) of our FCSEL's.

In conclusion, we have fabricated GSMBE-grown, 1.3-$\mu$m wavelength, strained MQW InP–InGaAsP etched-facet FCSEL's with a very low CW threshold current of 32 mA. To our knowledge, this is the first demonstration of high-performance, etched-facet, 1.3-$\mu$m FCSEL's. With wafer-level bonding on a heat sink, a surface-normal power in excess of 15 mW was achieved. Single longitudinal-mode operation with >15 dB side-mode suppression was observed. The simple and reproducible high-quality etching of the 45° and vertical facets in a conventional $CH_4$–$H_2$ RIE system made these FCSEL's attractive for applications that require monolithic integrated lasers with other InP-based optoelectronic devices.

## Acknowledgment

The authors thank M. J. Lange for his help in this work.

## References

[1] S. Yu and S. R. Forrest, "Implementations of smart pixels for optoelectronic processors and interconnection," *J. Lightwave Technol.*, vol. 11, pp. 1659–1669, 1993.
[2] J. J. Dudley, D. I. Babic, R. Mirin, L. Yang, B. I. Miller, R. J. Ram, T. Reynolds, E. L. Hu, and J. E. Bowers, "Low threshold, wafer fused long wavelength vertical cavity lasers," *Appl. Phys. Lett.*, vol. 64, pp. 1463–1465, 1994.
[3] D. I. Babic, J. J. Dudley, K. Streubel, R. P. Mirin, N. M. Margalit, J. E. Bowers, and E. L. Hu, "Double-fused 1.52 $\mu$m vertical-cavity lasers," *IEEE LEOS '94*, paper PD1.4, Boston, MA, Nov. 1994.
[4] C. Wu, M. Svilans, M. Fallahi, T. Makino, J. Glinsaki, C. Maritan, and C. Blaauw, "Optically pumped surface-emitting DFB GaInAsP/InP lasers with circular grating," *Electron. Lett.*, vol. 27, pp. 1819–1820, 1991.
[5] Z. L. Liau and J. N. Walpole, "Surface-emitting GaInAsP/InP laser with low threshold current and high efficiency," *Appl. Phys. Lett.*, vol. 46, pp. 115–117, 1985.
[6] H. Saito and Y. Noguchi, "A reflection-type surface-emitting 1.3 $\mu$m InGaAsP/InP laser array with microcoated reflector," *Jpn. J. Appl. Phys. Lett.*, vol. 28, pp. L1239–L1241, 1989.
[7] B. Stegmüller, H. Westermerier, W. Thulke, G. Franz, and D. Sacher, "Surface emitting InGaAsP/InP distributed feedback laser diode at 1.53 $\mu$m with monolithic integrated microlens," *Photon. Technol. Lett.*, vol. 3, pp. 776–778, 1991.
[8] H. P. Lee, A. Scherer, E. D. Beebe, W. P. Hong, R. Bhat, and A. A. Koza, "1.57 $\mu$m InGaAsP/InP surface emitting lasers by angled focus ion beam etching," *Electron. Lett.*, vol. 28, pp. 580–581, 1991.
[9] C.-P. Chao, G.-J. Shiau, and S. R. Forrest, "1.3 $\mu$m wavelength, InGaAsP/InP folded-cavity surface-emitting grown by gas source molecular beam epitaxy," *Photon. Technol. Lett.*, vol. 6, pp. 1406–1408, 1994.
[10] W. D. Goodhue, J. P. Donnelly, C. A. Wang, G. A. Lincoln, K. Rauschenbach, R. J. Bailey, and G. D. Johnson, "Monolithic two-dimensional surface-emitting strained-layer InGaAs/AlGaAs and AlInGaAs/AlGaAs diode laser arrays with over 50% differential quantum efficiencies," *Appl. Phys. Lett.*, vol. 59, pp. 632–634, 1991.

# Low-threshold 1.3-$\mu$m wavelength, InGaAsP strained-layer multiple quantum well lasers grown by gas source molecular beam epitaxy

Guang-Jye Shiau,[a] Chih-Ping Chao, Paul E. Burrows, and Stephen R. Forrest
*Advanced Technology Center For Photonics and Optoelectronic Materials, Department of Electrical Engineering, Princeton University, Princeton, New Jersey 08544*

(Received 5 April 1994; accepted for publication 3 June 1994)

We report the growth, by gas source molecular beam epitaxy (GSMBE) of low-threshold 1.3-$\mu$m wavelength strained-layer $In_{0.86}Ga_{0.14}As_{0.52}P_{0.48}/In_{0.86}Ga_{0.14}As_{0.3}P_{0.7}$ separate confinement heterostructure multiple quantum well lasers. Threshold currents as low as 16 mA were measured for a 390×5-$\mu$m ridge laser, and a threshold current density of $J_{th}$=490 A/cm$^2$ was achieved for a 1200×5-$\mu$m device. Apparently, this is the lowest value of $J_{th}$ reported to date for 1.3-$\mu$m lasers grown by GSMBE, and is comparable to the best devices grown by other techniques such as chemical beam epitaxy and metalorganic vapor phase epitaxy.

Gas source molecular beam epitaxy (GSMBE) using phosphine as the phosphorous source is suitable for growing InP-based optoelectronic devices, such as 1.3- and 1.55-$\mu$m wavelength quantum well lasers.[1] GSMBE is also capable of producing high-quality heterointerfaces, as required in quantum well lasers, owing to the fast gas switching and excellent control of the epitaxial layer thickness.[2] While high-quality GSMBE-grown 1.55-$\mu$m lasers have been reported,[3] to our knowledge, there have as yet been no reports of high performance GSMBE-grown 1.3-$\mu$m lasers. The challenge involved in growing 1.3-$\mu$m lasers is that two quaternary materials with different band gaps are usually required to be grown in a separate confinement heterostructure (SCH) to improve the optical confinement of the active waveguiding region. Of these two quaternary materials, the one with the larger band gap is for both the guiding and barrier layers, while the smaller band-gap material is for the quantum wells. The guiding quaternary must be lattice matched to the InP substrate to avoid the formation of misfit dislocations which results in excessive nonradiative recombination. On the other hand, strain can be intentionally incorporated into the quaternary wells to lower the threshold current.[4–7]

In this letter, we report the growth of 1.3-$\mu$m wavelength $In_{0.86}Ga_{0.14}As_{0.52}P_{0.48}/In_{0.86}Ga_{0.14}As_{0.3}P_{0.7}$ strained-layer multiple quantum well (MQW) lasers by GSMBE. A threshold current density of 490 A/cm$^2$ was achieved on a 1200×5-$\mu$m ridge laser. For a 390×5-$\mu$m ridge laser, a threshold current as low as 16 mA was measured.

The material was grown in a Riber CBE32 chamber equipped with a 2200-*l*/s turbomolecular pump and a CTI-8 cryopump. Elemental indium and gallium were used as the group III sources, while arsenic and phosphorous, obtained by cracking 100% pure arsine and phosphine, respectively, were used for the group V sources. The cracking temperature was 900 °C for both arsine and phosphine. The switching of hydride gases was performed in a run/vent design. Elemental beryllium and silicon were used as the *p*-type and *n*-type dopants, respectively. The growth chamber base pressure is $\sim 4\times10^{-10}$ Torr, and all source cells are kept at standby temperatures of from 450 to 600 °C.

Prior to growth, the substrate was degreased by boiling in 1,1,1-trichloroethane, followed by successive rinses in acetone and methanol. The sample was etched in a 3:1:1 $H_2SO_4:H_2O:H_2O_2$ solution and rinsed thoroughly in deionized water. The substrate was then loaded into the vacuum chamber immediately after being indium-bonded to a molybdenum holder. The substrate was outgassed at ~250 °C for 60 min to evaporate most of the volatile species prior to growth, followed by a thermal cleaning process at ~525 °C for 5–10 min inside the growth chamber under a phosphorous overpressure of $\sim 1.8\times10^{-5}$ Torr used to prevent surface decomposition. Reflection high-energy electron diffraction (RHEED) was used *in situ* to monitor the reconstruction of the substrate surface. RHEED patterns with continuous streaks were observed before as well as throughout the entire growth process indicating planar surfaces. The chamber pressure during growth was $1.8–2.6\times10^{-5}$ Torr, where a total hydride flow rate of 2.6–3.5 sccm was used. Typical growth rates were 0.9, 1.2, and 1.7 $\mu$m/h for InP, $In_xGa_{1-x}As_yP_{1-y}$ and $In_{0.53}Ga_{0.47}As$, respectively.

The laser structure, as shown in Fig. 1, was grown on a S-doped (100) InP substrate at a temperature of ~510 °C. First, a 1-$\mu$m-thick, $\sim 1\times10^{18}$ cm$^{-3}$ Si-doped InP buffer layer followed by a 300-Å-thick undoped InP spacer layer was grown. This, in turn, was followed by the growth of the undoped guiding and active layers. The active region, sandwiched between two 1000-Å-thick, lattice matched ($\Delta a/a=5\times10^{-4}$) $In_{0.86}Ga_{0.14}As_{0.3}P_{0.7}$ (band-gap cutoff wavelength $\lambda_g$=1.1 $\mu$m) guiding layers, consists of four compressively strained quantum wells. The wells consist of 67-Å-thick, $In_{0.86}Ga_{0.14}As_{0.52}P_{0.48}$, separated by barriers consisting of 100-Å-thick $In_{0.86}Ga_{0.14}As_{0.3}P_{0.7}$ layers. The well thickness (67 Å) is chosen so that the room-temperature peak photoluminescence (PL) wavelength of the quantum wells is ~1.3 $\mu$m, as required. A 300-Å-thick undoped InP spacer was grown, followed by a 1-$\mu$m-thick, $5\times10^{17}$ cm$^{-3}$ Be-doped InP upper cladding layer, and a 500-Å-thick $In_{0.53}Ga_{0.47}As$ contact layer with a Be concentration of $\sim 1–2\times10^{18}$ cm$^{-3}$.

In growing the MQW structures, the In/Ga flux ratio was

[a]Currently on leave from the Department of Materials Science, University of Southern California, Los Angeles, CA.


0003-6951/94/65(7)/892/3/$6.00
© 1994 American Institute of Physics

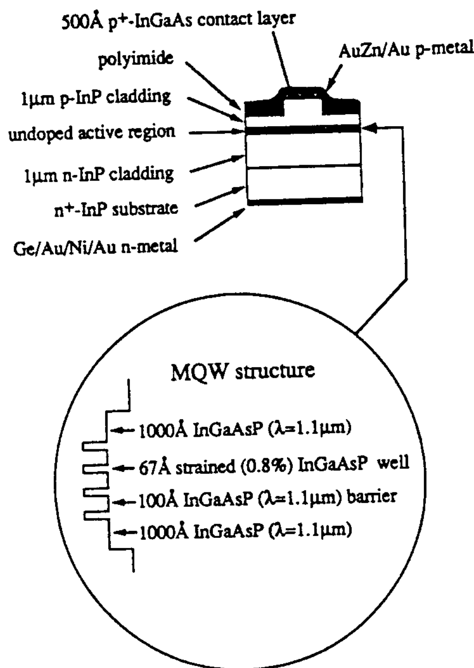


FIG. 1. Schematic structure of a 1.3-$\mu$m ridge waveguide laser diode. The material structure of the MQW active region is also shown.

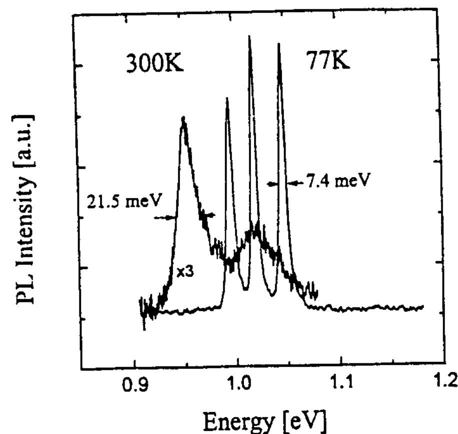


FIG. 2. Room-temperature and 77-K photoluminescence spectra of multiple single quantum well structure. Both spectra show very narrow linewidths of the QW structure.

kept constant while only the $As_2/P_2$ flux ratio was varied. A growth interruption of 15 s occurred during readjustment of the flow rates at every heterointerface. The use of growth interruptions has previously been found to eliminate surface roughening, thus improving the heterointerface quality.[8] The time interval (10 s) between closing the group III shutters and switching the group V gases served to smooth out islands and steps on the surface, while the other time interval (5 s) was used to re-equilibrate the flow for the next epitaxial layer. The latter time interval was kept short to avoid the As-P exchange[9] at the heterointerfaces. An additional evacuation time of 3 s was introduced into the growth interruption used for the InGaAs/InP heterojunctions, where a complete P/As flux change is required. A 3-s evacuation permitted an ~80% decrease of the chamber pressure, thus performing the P/As switching in a time sufficiently short to avoid surface decomposition.

Figure 2 shows room-temperature and 77-K PL spectra for a structure with 7-, 5.25-, and 3.5-nm nominal well widths, which served to calibrate the luminescence wavelength of the MQW structure. A thermally broadened full width at half maximum (FWHM) of 21.5 and 7.4 meV were obtained for room-temperature and 77 K PL, respectively, indicating that the grown materials are of very high quality. The strain of the well material was estimated to be +0.8% using double-crystal x-ray rocking curve measurements. It is worth mentioning that up to at least 20 Pendellösung fringes (see Fig. 3) were resolved in double-crystal x-ray rocking curve measurements of the laser structure, again, indicating the growth of layers with sharp heterointerfaces.

The device processing starts with the deposition of 5-$\mu$m-wide Ti stripes used as a mask for ridge etching. Citric acid was used to remove the top InGaAs layer, followed by removing ~8000-Å InP in a 1:10 diluted HBr solution. The Ti mask was then removed using buffered HF, and the top AuZn/Au $p$-contact was applied using a self-aligned polyimide planarization process. The wafer was lapped to a thickness of ~120 $\mu$m, followed by $e$-beam evaporation of the Ge/Au/Ni/Au $n$ contact on the substrate.

Light-current ($L$-$I$) characteristics for devices with cavity lengths ranging from 390 to 1200 $\mu$m were measured using a calibrated InGaAs detector. A typical $L$-$I$ curve for a 390×5-$\mu$m ridge as-cleaved waveguide laser is shown in Fig. 4(a). A threshold current of 16 mA was measured. The lasing wavelength was measured to be 1.302 $\mu$m at $I=I_{th}$ and shifts, due to device heating, to 1.304 $\mu$m at $I=2I_{th}$. The inset in Fig. 4(a) shows the laser emission spectrum measured at $I=22$ mA. The slope efficiency of the same device is 0.2 mW/mA per facet up to a 6 mW output power. For ridge lasers, the transparency current density is 320 A/cm$^2$, as obtained from a plot of threshold current density ($J_{th}$) versus inverse cavity length ($1/L$), as shown in Fig. 4(b). Furthermore, an internal quantum efficiency of 91% and a loss of 20 cm$^{-1}$ were measured. Also a threshold cur-

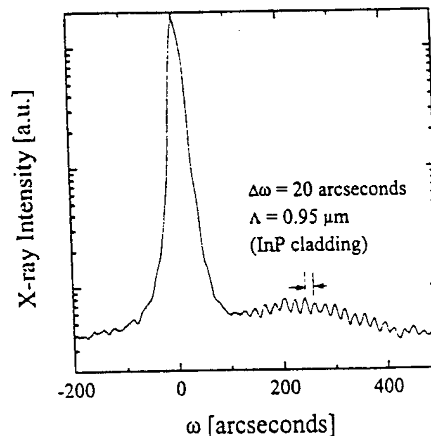


FIG. 3. A double-crystal x-ray diffraction rocking curve of the laser structure. Up to at least 20 Pendellösung fringes are resolved.

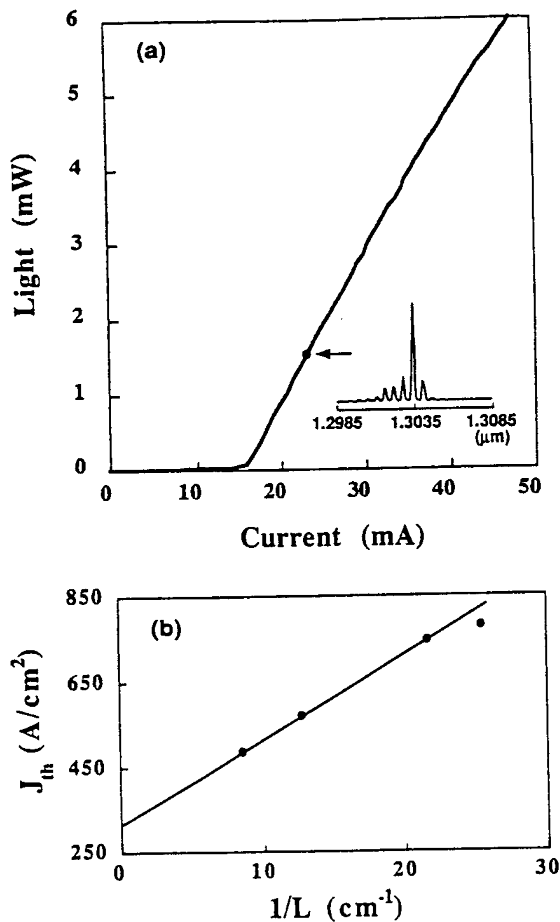


FIG. 4. (a) Light-current characteristic of a 390×5-$\mu$m ridge laser. Inset shows the lasing spectrum at $I=22$ mA. (b) Plot of threshold current density vs inverse cavity length.

rentdensity of 490 A/cm$^2$ was obtained on a 1200-$\mu$m-long ridge laser, which to our knowledge is the lowest reported to date for GSMBE-grown 1.3-$\mu$m lasers. This value is comparable to devices grown by other techniques. For example, Hausser *et al.*[10] have obtained a $J_{th}=400$ A/cm$^2$ for a 750-$\mu$m-long decoupled confinement heterostructure laser grown by chemical beam epitaxy (CBE). Imajo *et al.*[11] reported a $J_{th}=450$ A/cm$^2$ for a 900-$\mu$m-long, $InAs_yP_{1-y}/InP$ strained-layer MQW laser grown by metalorganic chemical vapor deposition (MOCVD).

Due to a smaller refractive index step and conduction-band offset between the barrier and well layers, a 1.3-$\mu$m $In_{x1}Ga_{1-x1}As_{y1}P_{1-y1}/In_{x2}Ga_{1-x2}As_{y2}P_{1-y2}$ laser usually suffers from inferior optical and electrical confinement compared to a 1.55-$\mu$m laser. By an appropriate design, and by employing strain into the well material, we have demonstrated that 1.3-$\mu$m lasers can still demonstrate very low threshold currents. In conclusion, we have described the growth of low-threshold, 1.3-$\mu$m wavelength, strained-layer $In_{0.86}Ga_{0.14}As_{0.52}P_{0.48}/In_{0.86}Ga_{0.14}As_{0.3}P_{0.7}$ separate confinement heterostructure MQW lasers by GSMBE. A threshold current as low as 16 mA was measured for a 390×5-$\mu$m ridge laser, and a threshold current density of 490 A/cm$^2$ was achieved for a 1200×5-$\mu$m device. To the best of our knowledge, these are the lowest values reported to date for 1.3-$\mu$m lasers grown by GSMBE.

The authors acknowledge RADC/ARPA, AFOSR, and U.S. Army CECOM for their support of this work.

[1] H. Q. Hou and C. W. Tu, J. Cryst. Growth **120**, 167 (1992).
[2] J. M. Vandenberg, S. N. G. Chu, R. A. Hamm, M. B. Panish, and H. Temkin, Appl. Phys. Lett. **49**, 1302 (1986).
[3] C. Starck, J.-Y. Emery, R. J. Simes, M. Matabon, L. Goldstein, and J. Barrau, J. Cryst. Growth **120**, 180 (1992).
[4] A. R. Adams, Electron. Lett. **22**, 249 (1986).
[5] E. Yablonovitch and E. O. Kane, IEEE J. Lightwave Technol. **LT-6**, 1292 (1988).
[6] J. P. Loehr and J. Singh, IEEE J. Quantum Electron. **27**, 708 (1991).
[7] D. Coblentz, T. Tanbun-Ek, R. A. Logan, A. M. Sergent, S. N. G. Chu, and P. S. Davisson, Appl. Phys. Lett. **59**, 405 (1991).
[8] J. Hergeth, D. Grützmacher, F. Reinhardt, and P. Balk, J. Cryst. Growth **107**, 537 (1991).
[9] H. Y. Lee, M. J. Hafich, G. Y. Robinson, K. Mahalingam, and N. Otsuka, J. Cryst. Growth **111**, 525 (1991).
[10] S. Hausser, C. S. Harder, H. P. Meier, and W. Walter, Appl. Phys. Lett. **62**, 663 (1993).
[11] Y. Imajo, A. Kasukawa, T. Namegaya, and T. Kikuta, Appl. Phys. Lett. **61**, 2506 (1992).

IEEE PHOTONICS TECHNOLOGY LETTERS, VOL. 8, NO. 1, JANUARY 1996



# Fabrication and Analysis of High-Contrast InGaAsP–InP Mach–Zehnder Modulators for Use at 1.55-μm Wavelength

M. Fetterman, C.-P. Chao, and S. R. Forrest

***Abstract*— A high-contrast ratio, low voltage-length product, multiple quantum well InGaAsP–InP Mach–Zehnder interferometer is demonstrated and analyzed. An on/off ratio of over 40 dB and voltage-length product of 1.8 V-mm were measured, results which are superior to previous reports of similar MQW structures. Using the Lanczos–Helmholtz beam propagation method, we find that the linear and quadratic electrooptic coefficients for InGaAsP quantum wells are $r = (3.9 \pm 1.7)$ pm/V and $s = (5.0 \pm 1.5) \times 10^{-19}$ m$^2$/V$^2$, respectively. We also demonstrate active optical alignment of the modulator guides using integrated waveguide light emitting diodes.**

## I. Introduction

HIGH-FREQUENCY modulation at a wavelength of $\lambda = 1.55$ μm is important for telecommunications and data communications [1]. External modulators such as the Mach–Zehnder (MZ) interferometer can operate at high frequencies, and can have relatively low chirp. Commercial MZ's are generally made from bulk $LiNbO_3$ crystals. On the other hand, semiconductor multiple quantum well (MQW) devices [2]–[5] that utilize the quantum confined Stark effect (QCSE) have a larger electrooptic coefficient than devices made from lithium niobate [6], leading to low switching voltages, reduced power consumption, and high bandwidths. Semiconductors also offer the potential for integration with other active optoelectronic components [7].

In this letter, a high-contrast ratio, low voltage-length product InP/InGaAsP MZ for use at a wavelength of $\lambda = 1.55$ μm is demonstrated. The 300-μm long device has a 6 V switching voltage, a switching voltage-length product of $V \cdot L = 1.8$ V-mm, and an on/off ratio $R > 40$ dB. These parameters, to our knowledge, exceed those reported to date [2]–[5]. The high $R$ value of this MZ is due to low absorption loss and balanced splitting between the arms of the Y-branches (YB's), and the low $V \cdot L$ product is a consequence of the strong electrooptic effect in the InGaAsP guiding layers and quantum wells. To accurately analyze this device, we apply and extend the Lanczos–Helmholtz Beam Propagation Method [8] (LHBPM) to calculate the optical overlap factor, and to study the splitting [9] in the arms of the YB. In addition, we introduce alignment electrodes which consist of light-emitting diodes (LED's) on

Manuscript received June 21, 1995; revised September 6, 1995.

The authors are with the Department of Electrical Engineering, Advanced Technology Center for Photonics and Optoelectronic Materials, Princeton University, Princeton, NJ 08544 USA.

Publisher Item Identifier S 1041-1135(96)00545-9.

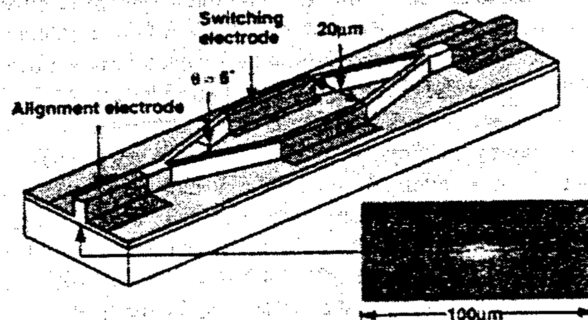


Fig. 1. Perspective schematic view of the Mach–Zehnder modulator. Inset. Image of the light spot emitted from an alignment electrode. Dimensions of the guided light from the electrode are on the order of (10 μm)$^2$.

the input and output of the modulator waveguides. They simplify the task of aligning the MZ waveguides with input and output optical fibers, and are useful for packaging and fiber pigtailing.

The MZ modulator structure, shown schematically in Fig. 1, has two YB's with a 6° separation angle, a 3 μm wide waveguide ridge, and active lengths that vary from 300–700 μm. The center-to-center spacing of the electrode arms is 20 μm, and the total device length is 2.5 μm. The alignment electrodes allow for active fiber alignment to the waveguide by forward biasing light emitting diodes (LED's) at both ends of the MZ. By placing a detector at the opposite end of the fiber pigtail, the MZ waveguide can be rapidly and accurately aligned to the output fiber. The light intensity pattern emitted from one of these diodes is shown in the inset of Fig. 1, and the dimensions of the light spot are on the order of 10 μm, clearly indicating guiding of the emitted light in the ridge region.

The wafer was grown by metalorganic chemical vapor deposition on (100) n$^+$ InP S-doped at $10^{18}$ cm$^{-3}$. The first layer is a 1-μm thick, S:InP buffer layer also doped to $10^{18}$ cm$^{-3}$, followed by a 0.1-μm thick, undoped InGaAsP cladding layer with an energy gap of $E_g = 1.08$ eV. The undoped quantum well region consists of 5 unstrained InGaAsP ($E_g = 0.90$ eV), 70-Å thick quantum wells, and 100-Å thick barriers with $E_g = 1.08$ eV. A second undoped, 0.1-μm thick InGaAsP buffer layer ($E_g = 1.08$ eV), a Zn:InP ($5 \times 10^{17}$ cm$^{-3}$) 1-μm thick waveguiding layer, and a 0.2-μm thick, Zn:InGaAs layer ($10^{19}$ cm$^{-3}$) for ohmic contact are grown on top.

1041-1135/96$05.00 © 1996 IEEE

To fabricate the waveguide device, a 1000-Å thick layer of $SiN_x$ is deposited using plasma enhanced chemical vapor deposition at a substrate temperature of 250 °C. The $SiN_x$ is then patterned as a 3-$\mu$m wide ridge etching mask. A 0.85 $\mu$m deep InGaAs–InP ridge was formed by reactive ion etching in a 550 V, $CH_4$–$H_2$ (1:6) plasma. Next, a 3000 Å thick $SiN_x$ contact isolation layer is deposited, and then removed prior to e-beam deposition of Ti–Pt–Au (200 Å/500 Å/3000 Å) electrodes. After the wafer was lapped to a thickness of 150 $\mu$m, a Ge–Au–Ni–Au (270 Å/450 Å/215 Å/1200 Å) n-metal contact was deposited on the substrate surface and the contacts were annealed at 360 °C for 90 s. The wafer was then cleaved into rows of devices, and a 1800-Å thick SiO anti-reflective layer was e-beam evaporated onto the cleaved facet surfaces.

Fig. 2 shows the (TE mode) MZ output intensity as a function of voltage for a 300-$\mu$m long device, indicating $R > 40$ dB (limited by the output detector sensitivity), and a switching voltage of 6 V, giving $V \cdot L = 1.8$ V-mm. In contrast, the TM mode had $R = 5$–10 dB. Modulators with lengths ranging from 300–700 $\mu$m showed similar performance of $R = 30$–40 dB and $V \cdot L$ in the range of 1.8–4 V-mm for TE modes. For comparison [3], similar GaAs–AlGaAs MZ devices have $R = 23.8$ dB and $V \cdot L = 5.5$ V-mm. InP–InGaAsP quantum well [2] MZ's have been demonstrated with $V \cdot L = 2.1$ V-mm and $R = 16$ dB. The fiber-to-fiber loss was measured to be 40 dB which is higher than the 31-dB insertion loss reported for a similar GaAs–AlGaAs MZ modulator using 1° Y-branches [3]. The higher loss is attributed, in part, to the larger branching angle of 6° used in this work. Also, some additional loss may be incurred due to the nonideal fiber-waveguide coupling of our experimental setup.

The capacitance and resistance of 300-$\mu$m long devices are 3.5 pF and 30 Ω, respectively. From these values, we estimate a 3-dB cut-off frequency of 1.5 GHz. However, the capacitance can be reduced by more than a factor of ten (and the frequency increased by a concomitant amount) by reducing the size of the electrode probing pads [3] and isolating the active and passive waveguide ridge regions.

The electroluminescence measured from the alignment electrode peaked at $\lambda = 1.32$ $\mu$m, implying that the absorption loss at the operating wavelength of $\lambda = 1.55$ $\mu$m is negligible. The data of Fig. 2 can, therefore, be fit using:

$$I(V) = I_0\{A^2 + B^2 + 2A^2B^2 \cos[\Delta n(V)kL + \phi]\}. \quad (1)$$

Here, $I(V)$ is the output intensity as a function of voltage, $I_0$ is the intensity at $V = 0$, $\Delta n(V)$ is the change of index of refraction as a function of voltage, $k = 2\pi/\lambda$, $L$ is the device length, and $\phi$ is a phase shift. The two YB's are characterized by the coefficients $A$ and $B$, where $A$ and $B$ are the intensities that couple into each arm following $A + B = 1$. The on/off ratio is then given by $R = 1/(A - B)^2$. For an on/off ratio of $R = 10^4$ as shown in Fig. 2, this implies that $A - B = 0.01$, from which we infer a YB asymmetry of <1%. With (1), and using $A = B = 0.5$, $\Delta n(V)$ is extracted from the fit to the data of Fig. 2. The dependence of $\Delta n$ on voltage and the corresponding theoretical fit are shown in the inset to Fig. 2.

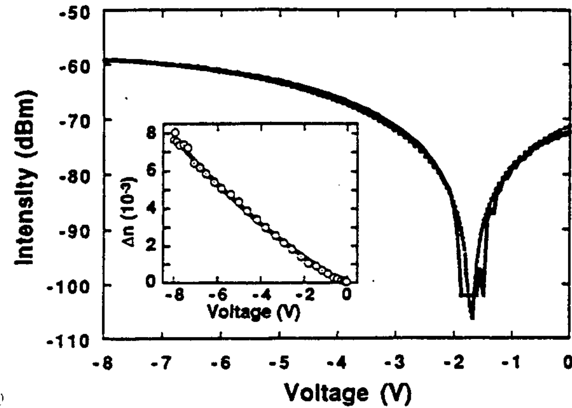


Fig. 2. The response of a 300 $\mu$m long Mach–Zehnder at $\lambda = 1.55$ $\mu$m. The on/off ratio is >40 dB and the switching voltage is 6 V. Dashed line is a theoretical fit to the data described in the text. Inset: Refractive index change, $\Delta n(V)$, obtained from the data of Fig. 2 (circles). Dashed line is a theoretical fit.

The index change is due to both the bulk (non-QW), $\Delta n_{\text{bulk}}$, and quantum well regions, $\Delta n_{qw}$, via $\Delta n = \Delta n_{qw} + \Delta n_{\text{bulk}}$. The value of $\Delta n_{\text{bulk}}$ is [10]:

$$\Delta n_{\text{bulk}} = \tfrac{1}{2}\Gamma_{\text{bulk}}\, n_0^3\,[r_{\text{bulk}}(E - E_0) + s_{\text{bulk}}(E - E_0)^2 + (r_{\text{bulk}}E_0 - s_{\text{bulk}}E_0^2)], \quad (2)$$

where $\Gamma_{\text{bulk}}$ is the optical confinement factor for the bulk region, $n_0$ is the refractive index with no applied field [11], $r_{\text{bulk}}$ and $s_{\text{bulk}}$ are the linear and quadratic electrooptic coefficients, respectively, $E$ is the applied electric field, and $E_0$ is the built-in junction electric field. The same form of expression is also used for $\Delta n_{\text{bulk}}$.

To accurately determine $\Gamma$, and hence, the coefficients $r$ and $s$, the LHBPM[8] was used to model the waveguide modes and YB splitting of the MZ. An exact solution of the Helmholtz equation used in modeling wave propagation generally considers the set of all possible waves propagating at each point of a grid in the $x$–$y$ plane perpendicular to the propagation direction, $z$, using a coupling matrix. However, this is often not possible to implement since grids consisting of the large number of points necessary to model structures with a complicated index profile, $n(x, y)$, such as the MQW MZ, require an extremely large coupling matrix. The LHBPM reduces the original extremely large coupling matrix to a subspace that only has a few elements, making the wave propagation problem soluble. In our calculations we used the wafer structure previously described with the following refractive indices [11]: $n_{\text{sub}} = 3.17$ (InP substrate), $n_{\text{barrier}} = 3.30$ (the InGaAsP cladding region and quantum well barriers are made of the same material), and $n_{qw} = 3.46$ (InGaAsP quantum wells) along with a five-dimensional Lanczos subspace. Grid spacings of $\Delta x = 0.15$ $\mu$m, $\Delta y = 25$ Å, and a propagation step increment of $\Delta z = 1$ $\mu$m were used. Often when modeling such structures, the index of refraction is taken to be the average of the quantum well and barrier materials. Here, the resolution of the grid was sufficient so that this approximation was not necessary.

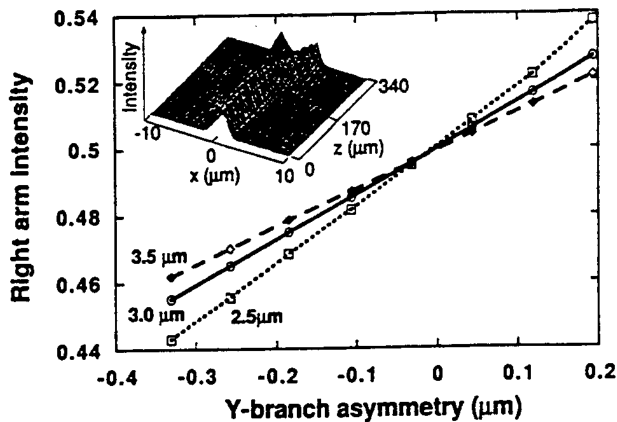


Fig. 3. The calculated fraction of power coupled into the right arm as a function of the difference in widths of an asymmetric Y-branch. The left arm is held fixed at the width indicated, and the right arm width is varied. Inset: Light intensity showing propagation in an asymmetric Y-branch.

Optical confinement factors of $\Gamma_{\text{bulk}} = 0.54$ and $\Gamma_{qw} = 0.12$ were calculated by the LHBPM. Previous work [2] has shown that $s_{\text{bulk}} = 0$ and that $r_{qw} = r_{\text{bulk}}$. With these assumptions and the data from the inset of Fig. 2, it is found that $r_{qw} = r_{\text{bulk}} = (3.9 \pm 1.7)$ pm/V and $s_{qw} = (5.0 \pm 1.5) \times 10^{-19}$ m$^2$/V$^2$. The dotted line in Fig. 2 fits the experimental data assuming these values for $r$ and $s$ and (1) and (2). This fit also gives $V_\pi = 6$ V. By comparison, the linear electrooptic coefficient of bulk GaAs[10] at $\lambda = 1.15$ $\mu$m is $r_{\text{bulk}} = 1.6$ pm/V and the quadratic electrooptic coefficient of a similar GaAs QW device [3] at $\lambda = 0.8$ $\mu$m is $s_{qw} = 1.3 \times 10^{-18}$ m$^2$/V$^2$.

The LHBPM was also used to study the coefficients $A$ and $B$ of the YB's [9], defined in (1). Fig. 3 shows the ratio of power coupled into the right YB arm as a function of the arm width difference, or YB waveguide asymmetry. The inset to Fig. 3 shows a plot of wave intensity as a function of position in a YB. In Fig. 3, the three curves correspond to waveguide widths of $W = 2.5$ $\mu$m, 3.0 $\mu$m, and 3.5 $\mu$m. The difference between the slope of the curves shows that, as expected, YB's constructed using wide waveguides are less sensitive to asymmetries than are narrow guides. When the width of the 3 $\mu$m guide used in our devices varies by 0.04 $\mu$m, then $A - B = 0.01$, implying that >40 dB on/off ratio is possible under these circumstances. Besides using balanced Y-branches, to achieve a high on/off ratio we also need to minimize voltage induced absorption changes which can lead to asymmetries in the intensity of the two waves at the output Y-branch. To accomplish this, we have a QW with an effective energy gap of 0.9 eV, which is further from the 1.55 $\mu$m operational wavelength than is typical for MQW MZ modulators [4]. In addition, operation far from the band edge accounts for the apparently low-quadratic electrooptic coefficient in our device. Nevertheless, at an operational voltage of 3 V, about one third of the total index change comes from the quadratic electrooptic effect.

In conclusion, we fabricated and analyzed a high-contrast ratio, low switching-voltage InGaAsP MQW MZ modulator for use at $\lambda = 1.55$ $\mu$m. A 300 $\mu$m long device has a 6 V switching voltage, $V \cdot L = 1.8$ V-mm, and $R > 40$ dB. These parameters, to our knowledge, exceed those reported to date [2]–[4]. The electrooptic coefficients of the InGaAsP QW material were measured and analyzed using the highly accurate Lanczos–Helmholtz beam propagation method, and are found to be $r = (3.9 \pm 1.7)$ pm/V and $s = (5.0 \pm 1.5) \times 10^{-19}$ m$^2$/V$^2$ for the linear and quadratic electrooptic coefficients at 1.55 $\mu$m, respectively. Effects of waveguide asymmetry are also studied using this model. The high R-value of this MZ is due to low-absorption loss and extremely even splitting between the arms of the YB's. We demonstrate novel active waveguide input/output electrodes, which make fiber alignment to waveguide devices faster and more accurate than current passive alignment methods.

## ACKNOWLEDGMENT

The authors thank US Army CECOM and ARO for their support of this work.

## REFERENCES


[1] A. B. Buckman, *Guided-Wave Photonics*. Orlando, FL: Saunders College Publishing, 1992.

[2] J. E. Zucker, K. L. Jones, B. I. Miller, and U. Koren, "Miniature Mach–Zehnder InGaAsP quantum well waveguide interferometers for 1.3 $\mu$m," *IEEE Photon. Technol. Lett.*, vol. 2, pp. 1041–1043, 1990.

[3] S. Cites and P. R. Ashley, "High-performance Mach–Zehnder modulators in multiple quantum well GaAs/AlGaAs," *J. Lightwave Technol.*, vol. 12, pp. 1167–1173, 1994.

[4] N. Agrawal, D. Franke, C. M. Weinert, H.-J. Ehrke, G. G. Mekonnen, D. Franke, C. Bornholdt, and R. Langenhorst, "Fast 2 × 2 Mach–Zehnder optical space switches using InGaAsP-InP multiquantum-well structures," *IEEE Photon. Technol. Lett.*, vol. 7, pp. 644–645, 1995.

[5] K. Wakita, I. Kotaka, and H. Asai, "High-speed InGaAlAs/InAlAs multiple quantum well electrooptic phase moduators with bandwidth in excess of 20 GHz," *IEEE Photon. Technol. Lett.*, vol. 4, pp. 16–18, 1992.

[6] T. Fujiwara, A. Watanabe, and H. Mori, "Measurement of uniformity of driving voltage in Ti : $LiNbO_3$ waveguides using Mach–Zehnder interferometers," *IEEE Photon. Technol. Lett.*, vol. 2, pp. 260–262, 1990.

[7] T. L. Koch, "Semiconductor photonic integrated circuits," *J. Quantum Electron.*, vol. 27, pp. 641–643, 1991.

[8] R. P. Ratowsky and J. A. Fleck, Jr., "Accurate numerical solution of the Helmholtz equation by iterative Lanczos reduction," *Opt. Lett.*, vol. 16, pp. 787–789, 1991.

[9] H. P. Chan, P. S. Chung, and E. Y. B. Pan, "Mode conversion in Y-branch waveguides," in *SPIE, Integrated Optical Circuits*, vol. 1583, pp. 129–132, 1991.

[10] A. Yariv and P. Yeh, *Optical Waves in Crystals*. New York: Wiley, 1983.

[11] B. Broberg and S. Lindgren, "Refractive indices of InGaAsP," *J. Appl. Phys.*, vol. 55, pp. 3376–3381, 1984.

APPENDIX C

# Monolithic Integration of an InGaAsP/InP MQW Laser/Waveguide Using a Twin-Guide Structure with a Mode Selection Layer

L. Xu, M. R. Gokhale, P. Studenkov, J. C. Dries, C.-P. Chao, D. Garbuzov, and S. R. Forrest

Advanced Technology Center for Photonics and Optoelectronic Materials

Department of Electrical Engineering and Princeton Materials Institute

Princeton University, Princeton, NJ 08544

## Abstract

We demonstrate a monolithically integrated 1.55 μm wavelength InGaAsP/InP multiple quantum well laser with a passive Y-branch waveguide in a vertical twin-waveguide structure. To reduce the sensitivity of the device performance characteristics to laser cavity length and variations in the layer structure, we introduce an $In_{0.53}Ga_{0.47}As$ absorption, or "loss" layer. This layer eliminates the propagation of the even mode, while having minimal effect on the odd mode. The threshold current densities and differential efficiencies of the devices are unaffected by the loss layer. A record high coupling efficiency of 45% from the laser to the external passive waveguide is obtained.

# Monolithic Integration of an InGaAsP/InP MQW Laser/Waveguide Using a Twin-Guide Structure with a Mode Selection Layer

L.Xu, M. R. Gokhale, P. Studenkov, J. C. Dries, C.-P. Chao, D. Garbuzov, and S. R. Forrest

Advanced Technology Center for Photonics and Optoelectronic Materials

Department of Electrical Engineering and Princeton Materials Institute

Princeton University, Princeton, NJ 08544

Photonic integrated circuits (PICs) have the potential for producing low cost, high performance, advanced devices for optical communication. An important building block for PICs is a laser coupled to a passive waveguide, which is essential for monolithic integration of lasers with modulators, splitters, and efficient couplers to optical fibers. A laser can be integrated with a passive waveguide using a number of different techniques, including regrowth with separate optimization of the two devices [1], single growth on an etched substrate [1], disordering of multiple quantum wells (MQW) to locally change the bandgap [2], selective area growth enhancement using organometallic vapor phase epitaxy [3], or evanescent optical field coupling in a vertical twin-waveguide (TG) structure [4, 5, 6]. This last approach is attractive as a versatile "platform" technology for PICs, since a single growth step produces a structure on which a variety of active (e.g. lasers and optical amplifiers) and passive (e.g. waveguides and couplers) devices can be fabricated. Suematsu, et al. [5] demonstrated the first TG laser consisting of vertically integrated active and passive waveguide layers which were phase-matched in a manner similar to a directional coupler [7, 8]. Recently, a GaAs/AlGaAs-based TG laser integrated with a Y-branch single mode ridge waveguide was demonstrated [6]. However, that simple structure was so sensitive to variations in the device structure that the threshold current and coupling to the passive waveguide were practically uncontrollable [9]. The problem arises from the interaction between the even and odd modes in the conventional TG structure. Due to this interaction, the fraction of the total optical power incident on the etched facet of the active waveguide is a periodic function of cavity

length, which makes it extremely difficult to control the amount of power reflected from the etched facet. Furthermore, the modal gain and the coupling length both vary dramatically with changes in composition and thickness of each layer.

In this letter we describe monolithic integration of a 1.55 μm wavelength, InP/InGaAsP MQW laser with a passive Y-branch waveguide using a vertical TG structure with mode selectivity. We introduce an $In_{0.53}Ga_{0.47}As$ absorption, or "loss layer", midway between the active and passive waveguides to suppress lasing on the even mode, thereby making the TG facet reflectivity and coupling efficiency independent of length.

Figure 1 shows a schematic cross-section of the device. The TG structure, operating at $\lambda$=1.55μm, has two stacked waveguiding layers separated by a coupling layer. The upper waveguide incorporates a multiple quantum well (MQW) active region, and the lower InGaAsP waveguide is passive. The structure, grown in a single epitaxial step on a (100) n-type InP:Si substrate by gas source molecular beam epitaxy (GSMBE), is summarized in Table I. The active region has three, 13 nm thick, InGaAsP quantum wells separated by 20 nm InGaAsP barriers with a bandgap of 1.0 eV. The large-bandgap passive waveguide is a 430 nm thick, undoped InGaAsP layer with $E_g$=1.0 eV. The two guides are separated by a 600 nm thick InP spacer layer. For devices with a loss layer, the spacer contains a 100 Å thick, undoped $In_{0.53}Ga_{0.47}As$ ($E_g \approx 0.75$ eV) absorption layer centered between two 300 nm thick InP layers.

The structure was designed such that the propagation constants and the QW optical confinement factors for both the even and odd modes are approximately equal. This ensures that both modes propagate at the same velocity, and the exchange of power between the guides is nearly complete in the absence of the loss layer [9]. The modal intensity and index profile in the twin-guide structure with a loss layer are shown in the inset of Fig. 1. At the center of the InP layer separating the two guides, the light intensity of the odd mode is zero while that of the even mode is comparable to the intensity in the guide layers. For a 100 Å thick InGaAs loss layer centered at this point, the confinement

factors of the even and odd modes in this layer are calculated to be 0.3% and $4 \times 10^{-4}$ %, respectively. Assuming an absorption of $10^4$ cm$^{-1}$ at $\lambda = 1.5$ μm in $In_{0.53}Ga_{0.47}As$ [10], the loss due to this layer for the even and odd modes is 30 cm$^{-1}$ and 0.04 cm$^{-1}$, respectively. Since both modes have approximately the same confinement factor (4.06%, 4.08%) in the active QW region, the odd mode reaches the lasing condition at lower current and hence will be favored. The intensity of light in both guides is nearly the same for the remaining odd mode, allowing for an output coupling at the etched facet of ≈50% while maintaining a reasonably low threshold current density.

We fabricated several integrated TG laser/waveguide devices with one cleaved facet and the second facet formed by dry etching. The device fabrication procedure is as follows. First, the laser region is protected by a ~300 nm thick $SiN_x$ mask, and reactive ion etching in a 1:7 $CH_4$:$H_2$ mixture is used to form a smooth vertical laser facet [11]. The facet etch is halted midway between the upper and lower guides, as shown in the scanning electron micrograph in Fig. 2. Next, wet etching is used to define the laser and passive waveguide ridges. The passive waveguide is angled at 7° with respect to the cleaved facet to reduce reflections back into the laser cavity. After p- and n-contact metallization, devices with different active region lengths are formed by cleaving the side opposite to the etched facet.

Figure 2 (a) shows the near field pattern from the cleaved facet of a TG device with loss layer. The light intensity from the upper and lower waveguides is approximately equal, and the center region is dark as expected for lasing only in the odd mode. Figure 2(b) shows the near field at the cleaved facet of the passive Y-branch waveguide. Approximately 45% of the light is coupled from the laser into the passive waveguide, as measured using an integrating sphere with the etched facet carefully masked. This is in excellent agreement with our calculations, and represents a significant increase in TG coupling compared with a previously reported value of ~13% [7] for a conventional TG device.

The calculated far-field pattern in Fig. 3(a) (dashed line) is a linear superposition of the odd and even modes. Experimental data clearly show that without the loss layer, lasing occurs on both modes. However, for a TG laser with InGaAs loss layer, the far-field pattern in Fig 3(b) matches the calculation for the odd mode with no contribution from the even mode. This confirms that the loss layer eliminates the even mode. As a result, both the coupling efficiency from the laser to the passive waveguide and the reflection from the etched facet are *independent of the laser cavity length*. The irregular threshold current variation with cavity length in a conventional TG laser, observed in Refs. [7] and [9], is completely eliminated using the loss layer.

Figures 4(a) and 4(b) show the threshold current density and inverse external efficiency versus cavity length for double-cleaved 3QW TG lasers with and without the loss layer. Also shown for comparison are results for a conventional 3QW, 1.55 μm Fabry-Perot laser grown by the same GSMBE process. It can be seen that, within experimental accuracy, the loss layer does not affect the TG laser performance. Note that the minimum threshold current densities of TG lasers are higher than that of Fabry-Perot lasers, since the optical mode in TG structure spans across both waveguides, and the quantum well confinement factor is correspondingly smaller. From the external efficiency data shown in Fig. 4(b), the internal losses for TG lasers with and without loss layers are similar but are higher than for conventional lasers. This is partly due to the increased free carrier absorption loss in the doped passive waveguide. For TG lasers with loss layer, we measured a maximum external efficiency of $\eta$ = 25% (L = 1.2 mm) and a lowest threshold current density of $J_{TH}$ = 720 A/cm$^2$ (L = 2 mm), as compared to values for conventional single waveguide lasers of $\eta$ = 50% (L = 0.75 mm) and $J_{TH}$ = 250 A/cm$^2$ (L = 2 mm).

In conclusion, we demonstrated an InGaAsP/InP, 1.55 μm wavelength, MQW laser monolithically integrated with a passive waveguide Y-coupler using a vertical twin-guide structure. It is shown for the first time that a loss layer placed between the two

waveguides eliminates the even mode while having little effect on the odd mode. With only the odd mode present, optical feedback from the etched facet and coupling to the external passive waveguide are independent of cavity length and structure variations. Such a modified twin-guide structure is an important step toward realizing a highly versatile, "platform" technology where a variety of active and passive devices can be monolithically fabricated on a single wafer structure.

The authors thank DARPA (A. Husain) and US Army CECOM (L. Coryell and J. Wright) for their support of this work.

**Figure captions**

**Figure 1** Schematic diagram of the twin waveguide structure with passive waveguide. Inset: Refractive index and calculated mode profiles in the TG structure with InGaAs loss layer.

**Figure 2** (a) Near field optical intensity pattern of a twin-guide laser with absorption layer as observed from the cleaved facet, (b) Near field pattern of the Y-branch output. The scanning electron micrograph shows the etched facet of TG laser and Y-branch passive waveguide.

**Figure 3** Polar plot of the measured (solid squares) and calculated (dashed line) far field pattern of TG lasers: (a) without InGaAs loss layer, and (b) with InGaAs loss layer.

**Figure 4** (a) Threshold current density, and (b) inverse efficiency as a function of cavity length, for double-cleaved TG lasers with and without absorption layer. Data (solid squares) for conventional 3QW lasers is shown for comparison.

## References

[1] L. Menigaux, D. Remiens, L. Dugrand, P. Sansonetti, A. Carenco, "A new monolithic laser waveguide butt-coupling scheme based on a single-step MOVPE," *Proc. 11th IEEE Int. Semicond. Laser Conf.*, Boston, MA, Aug. 29-Sept. 1, pp. 172-173, 1988.

[2] R.L. Thornton, W.J. Mosby, and T.L. Paoli, "Monolithic waveguide coupled cavity lasers and modulators fabricated by impurity induced disordering," *J. Lightwave Technol.*, vol. 6, pp. 786-792, 1988.

[3] T. Sasaki, M. Yamaguchi and M. Kitamura, "Monolithically integrated multi-wavelength MQW-DBR laser diodes fabricated by selective metalorganic vapor phase epitaxy," J. Cryst. Growth, vol. 145, pp. 846-851, 1994.

[4] R.K. Watts, "Evanescent field of thin field laser and passive waveguide," J. Appl. Phys., vol. 44, pp. 5635-5636, 1973.

[5] Y. Suematsu, M. Yamada and K. Hayashi "A multi-hetero AlGaAs laser with integrated waveguide," *Proc. IEE (lett)*, vol. 63, pp. 208-209, 1975.

[6] K. Okamoto, A. Yamada, Y. Nakano and K. Tada, "Design and fabrication of monolithically integrated lateral-electrode etched-mirror laser with Y-branch single-mode waveguide in GaAs/AlGaAs," Jpn. J. Appl. Phys. Vol 34, part 1, pp. 4809-4814, Sept. 1995.

[7] K. Utaka, Y.Suematsu, K.Kishino and H. Kawanishi, "Measurement of coupling coefficient and coupling length of GaAs/AlGaAs integrated twin-guide injection lasers prepared by liquid-phase-epitaxy", *Trans. IECE Japan*, vol. E62, pp. 319-323, 1979.

[8] M. Yamada, H. Nishizawa and Y. Suematsu, "Mode selectivity in integrated twin-guide lasers", *Trans. IECE Japan*, vol. E59, pp. 9-10, 1977.

[9] H. Ribot, P. Sansonetti, and A. Carneco, "Improved design for the monolithic integration of a laser and an optical waveguide coupled by an evanescent field," *IEEE J. of Quantum Electron.*, vol. 26, pp. 1930-1941, 1990.

[10] S. Adachi, "Physical properties of III-V semiconductor compounds - InP, InAs, GaAs, GaP, InGaAs, and InGaAsP," John Wiley & Sons, 1992

[11] C.-P. Chao, D. G. Garbuzov, G. J. Shiau and S. R. Forrest, "Low threshold, high power, 1.3 μm wavelength, InGaAsP/InP etched-facet folded cavity surface emitting lasers", IEEE Photonics Tech. Lett. Vol. 7, pp. 836-837, 1995.

Table 1: Layer structure of twin-guide laser with absorption layer

| **Layer Description** | **Composition** | **Effective Bandgap (eV)** | **Layer Thickness (nm)** |
|---|---|---|---|
| Substrate | $n^{+}$-InP:S | 1.36 | - |
| n-Cladding | n-InP:Si | 1.36 | 500 |
| Passive Waveguide | n-$In_{0.2}Ga_{0.8}As_{0.44}P_{0.56}$ | 1.0 | 430 |
| Coupling layer | n-InP:Si | 1.36 | 300 |
| Loss layer | $In_{0.53}Ga_{0.47}As$ | 0.77 | 10 |
| Coupling layer | n-InP:Si | 1.36 | 300 |
| Separate Confinement | i-$In_{0.2}Ga_{0.8}As_{0.44}P_{0.56}$ | 1.0 | 113 |
| Active QW region | $In_{0.2}Ga_{0.8}As_{0.7}P_{0.3}$ (QW) / $In_{0.2}Ga_{0.8}As_{0.44}P_{0.56}$ Barriers | 0.8 (well) 1.0 (barrier) | 3 X 13 (well) / 20 (barrier) |
| Separate Confinement | i-$In_{0.2}Ga_{0.8}As_{0.44}P_{0.56}$ | 1.0 | 113 |
| p-Cladding | p-InP:Be | 1.36 | 110 |
| Etch-stop layer | p- $In_{0.2}Ga_{0.8}As_{0.44}P_{0.56}$:Be | 1.0 | 51 |
| p-Cladding | p-InP:Be | 1.36 | 1000 |
| p-contact layer | $p^{+}$- $In_{0.53}Ga_{0.47}As$:Be | 0.75 | 70 |

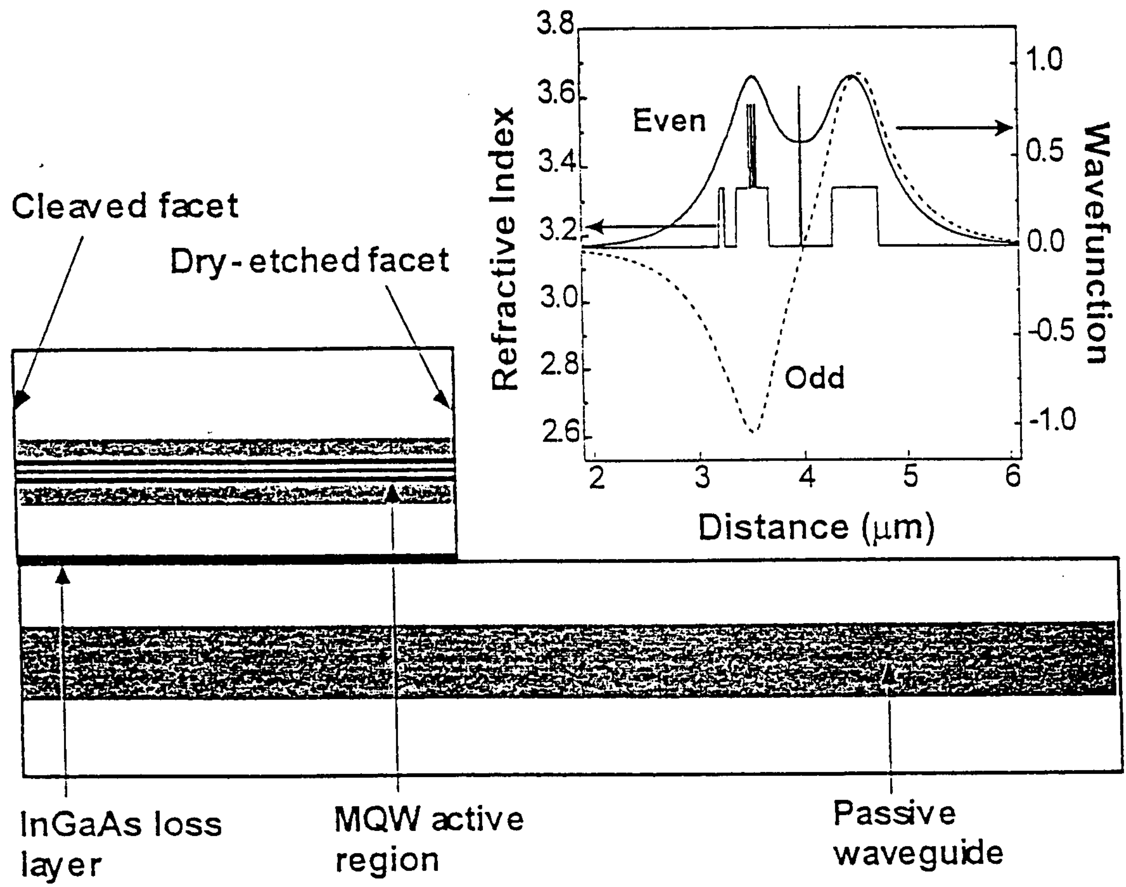


Figure 1

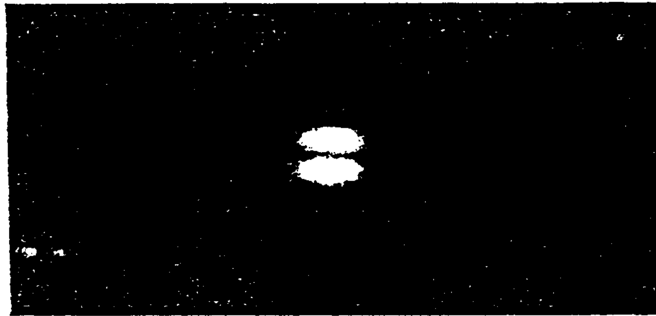

(a)

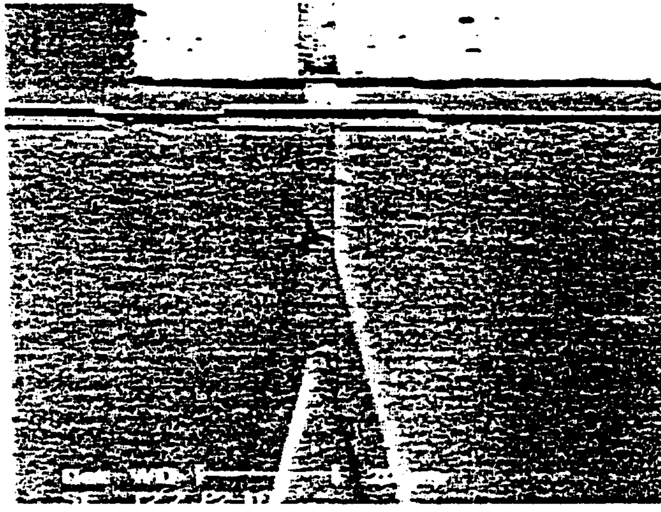

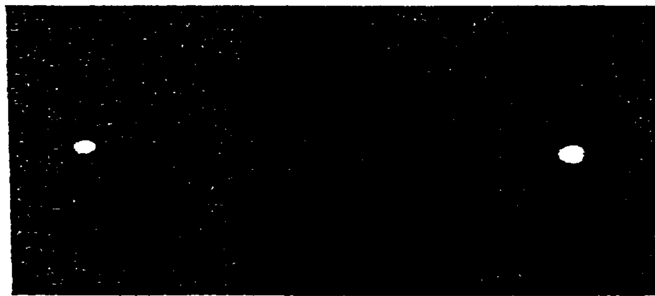

(b)

Figure 2

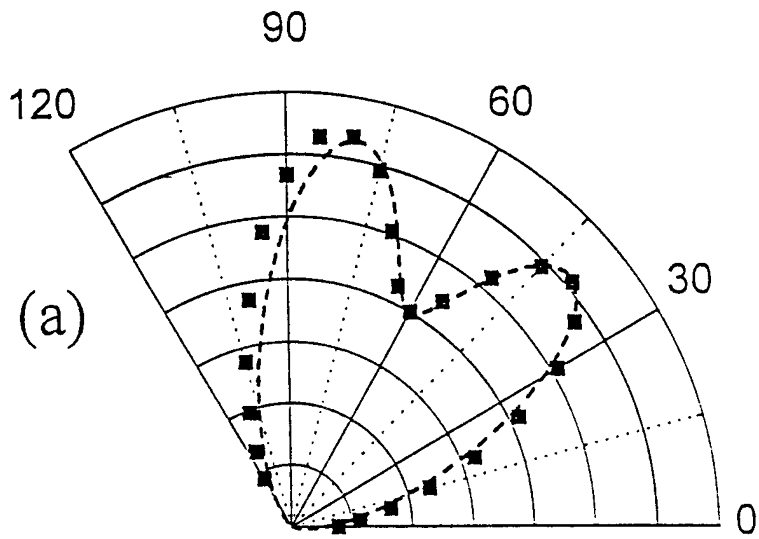


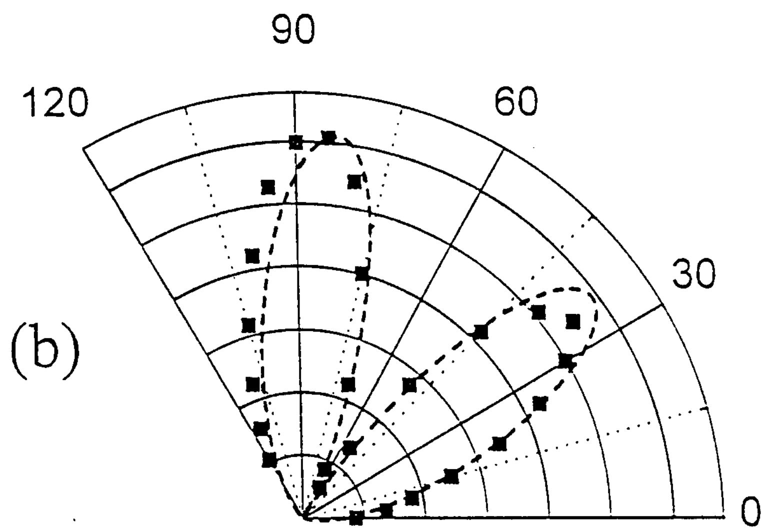


Figure 3

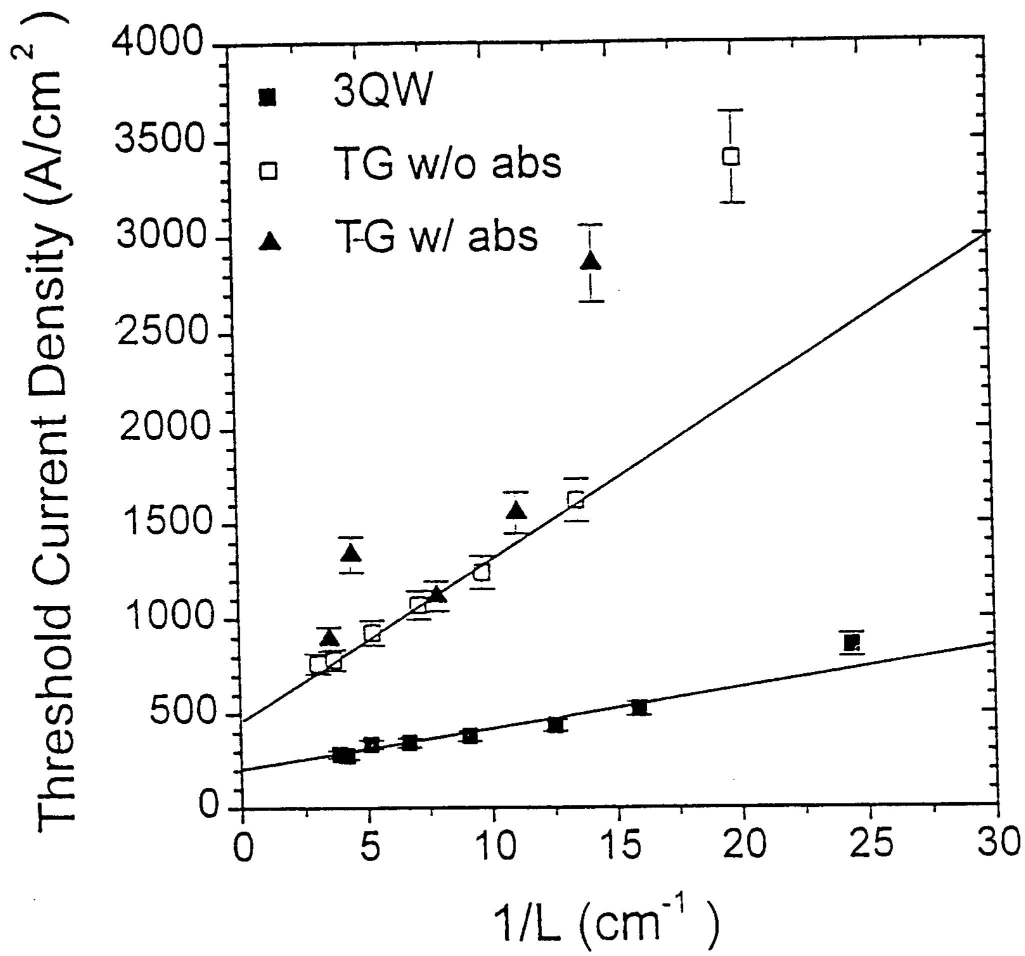


Figure 4(a)

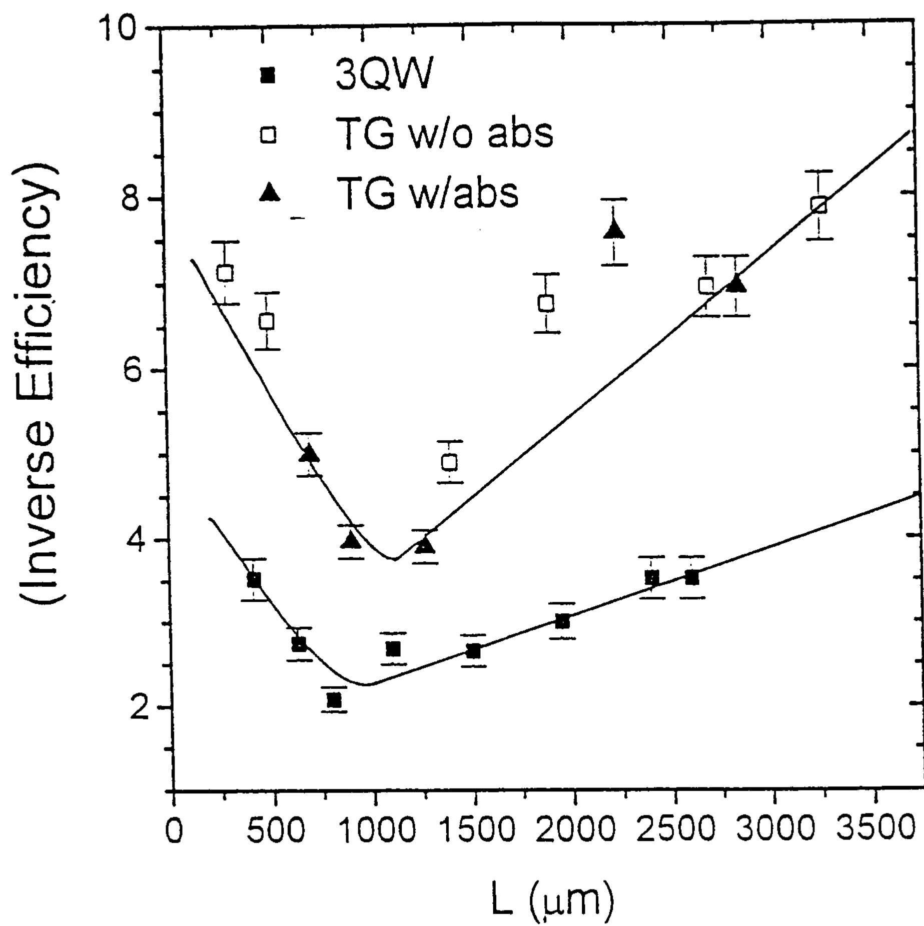


Figure 4(b)

APPENDIX D

# Technologies for Large Scale InP-based Optoelectronic Integrated Circuits

*Reprinted from*

# *Optoelectronic Integrated Circuits*

12–14 February 1997
San Jose, California

SPIE—The International Society for Optical Engineering

Volume 3006

©1997 by the Society of Photo-Optical Instrumentation Engineers
Box 10, Bellingham, Washington 98227 USA. Telephone 360/676-3290.

Invited Paper

# Technologies for Large Scale InP-based Optoelectronic Integrated Circuits

S. R. Forrest, D. S. Kim, S. Yu, J. Thomson, L. Xu, M. Gokhale, J. C. Dries, D. Garbuzov and P. Studenkov
Center for Photonics and Optoelectronic Materials (POEM)
Department of Electrical Engineering
Princeton University
Princeton, NJ 08544

M. Lange, G. H. Olsen and M. Cohen
Sensors Unlimited
3490 US Route 1
Princeton, NJ 08540

## ABSTRACT

We discuss approaches to achieving large scale InP-based optoelectronic integrated circuits (OEICs) and photonic integrated circuits (PICs). During the past several years, significant advances have been made in improving materials and device quality of InP-based materials such as InGaAs(P) for use in long wavelength communications systems and networks. Hence, we are currently on the threshold of realizing large scale (>500 device) OEICs from which will emerge a new generation of optoelectronic systems and applications, in analogy to what was achieved in the 1970's with the advent of Si-based electronic LSI. What remains to be demonstrated to bring this vision to practical reality is the demonstration of "platform" integration technologies where devices and circuits custom- designed for a wide range of applications can be realized using a common (and simple) epitaxial materials structure and fabrication process. For the last several years, we have developed such platform technologies, with our latest success being the demonstration of a 16x16 InGaAs/InP imaging array consisting of 272 field effect transistors and 256 p-i-n detectors. Other devices which have been demonstrated using this technology have been very high sensitivity switched photodiode receivers, and coherent optical receivers. The transmitter technology consists of a modified twin waveguide structure which allows for fabrication tolerant fabrication of photonic integrated circuits employing any combination of lasers, optical amplifiers, modulators and waveguides. The extremely high yield and simplicity of processing of such InP-based LSI circuits suggests that the scale of optoelectronic integration in this important materials system has reached a new, and highly useful level of sophistication.

## 1.0 INTRODUCTION

CMOS VLSI is unquestionably the dominant electronic integration technology in use today primarily due to the ease with which extremely complex circuits can be readily integrated using a common, well-developed fabrication process matched to equally sophisticated and accurate CAD tools. While the performance of CMOS circuits is high, it is, by no means, at the level of the highest performance circuits of which Si electronics are ultimately capable. Rather, CMOS technology is focused on addressing the broadest spectrum of applications, relying on special purpose integration technologies to address those particular uses. For this reason, almost all electronic computing systems today have adopted CMOS as their central platform integration technology. In effect, the extreme versatility of this device and materials technology has "driven" the development of a

plethora of new applications -- a point of view which is often ignored when considering modern photonic device and systems technologies.

With this historical perspective in mind, for the last ten years our laboratory has focused on developing photonic integrated circuit technologies which are capable of addressing the broadest range of applications, leaving the highest performance applications in the domain of independently optimized integration methods[1-6]. The result of this work has been the development of highly versatile, simple to implement integration technologies based on InP and related compounds for use over the wavelength band of 0.95 - 1.65 μm. Two separate integration technologies have been demonstrated: an optoelectronic integrated circuit (OEIC) "platform" based on InP/InGaAs p-i-n diodes and junction field effect transistors (JFETs) which generates a wide range of optical receiver configurations, and a photonic integrated circuit (PIC) platform for simply realizing complex laser, semiconductor amplifier (SOA), waveguide and modulator circuits. The OEIC technology has been used to fabricate large scale focal plane imaging arrays consisting of 272 field effect transistors and 256 p-i-n detectors, representing an important step toward realizing InP-based LSI. The PIC circuits have recently been used to develop an integrated laser/Y-branch optical circuit without any semiconductor regrowth, and with nearly 50% optical coupling between the integrated optical components.

In this paper, we will discuss example integrated devices based on these versatile integration technologies.

## 2.0 RECEIVERS AND ARRAYS USING P-I-N/JFET OEICS

A profile view of the platform wafer[6] is shown in Fig. 1. It consists of three layers (an undoped InP layer, thickness = 0.3 μm; an undoped $In_{0.53}Ga_{0.47}As$ layer, thickness = 1.5μm; and an n+InP layer, thickness=0.2μm and doping = $2x10^{18}cm^{-3}$) forming the p-i-n photodiode structure, followed by two layers (an undoped InGaAs spacer and etch-stop layer, thickness=0.5μm; a $8x10^{16}cm^{-3}$ n-type InGaAs channel layer, thickness=0.15μm; and an undoped InP cap layer, thickness=0.5μm) which form the InGaAs JFETs. This entire structure is grown on semi-insulating (100) Fe:InP substrates.

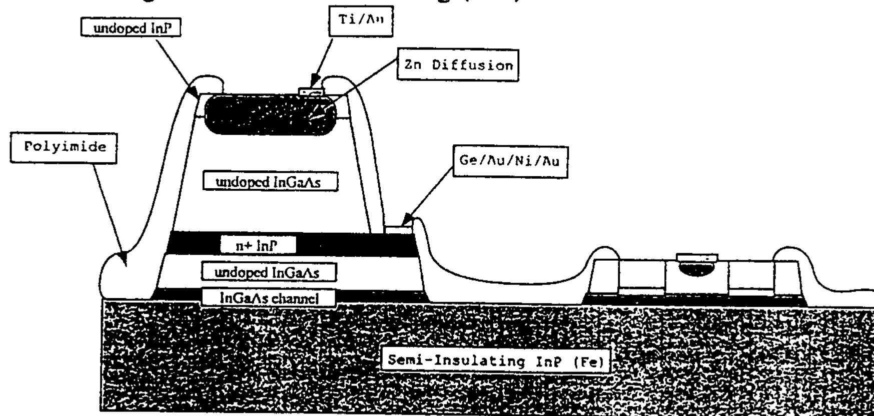


*Fig. 1: Cross-sectional view of the wafer structure used in the receiver OEIC.*

Processing this material into a receiver circuit begins by first etching down to the JFET layers using the InGaAs etch-stop layer to ensure uniform layer exposure. The etchant use with a large differential etch rate for InP as compared with InGaAs is $HBr:H_2O_2$ 10:1 diluted 10:1 in $H_2O$. The transistors are then isolated by a second etch down to the SI substrate. Next, a 1000Å layer of $SiN_x$ is deposited to serve as a junction diffusion mask.

Both the JFET gate and p-i-n detector junctions are simultaneously diffused through patterned holes in the mask using a sealed ampoule process at 500°C for approximately 30 min. Typically, JFET gate diffusion windows vary from 2 to 10 μm in length by 10 to 100μm in width. This represents the only critical process step, since the junction diffusion must be terminated near the interface between the InGaAs spacer and channel layers. We note, nevertheless, that the tolerances are relatively relaxed owing to the low doping of the spacer layer. That is, with low enough doping, the built-in depletion region extending from the p-n junction into the spacer will reach the channel layer without further application of voltage. A second SiNx layer is applied at this point which serves as the detector anti-reflection coating. Conventional metallizations to the n- and p- regions are made using e-beam evaporated Ge/Au/Ni/Au and Ti/Au, respectively, and alloyed in a rapid thermal annealer, followed by spin-on polyimide planarization of the small surface topography created by the transistor exposure and isolation etches. Holes are opened in the polyimide, and the final step is deposition of the Ti/Au device interconnection metals. The entire process sequence requires ten to fourteen mask levels, depending on details of the circuits being fabricated.

A recently demonstrated p-i-n/JFET receiver circuit[6] consisting of a 1x4 detector/JFET switching array at the front end is shown in Fig. 2. This receiver consists of eleven transistors, four photodiodes and three p-n junctions (corresponding to the JFET gate-source junction). We note that there are no resistors or capacitors on this circuit: all resistances are active loads (Q5, Q8, Q10), or are voltage-tunable loads (Q11).

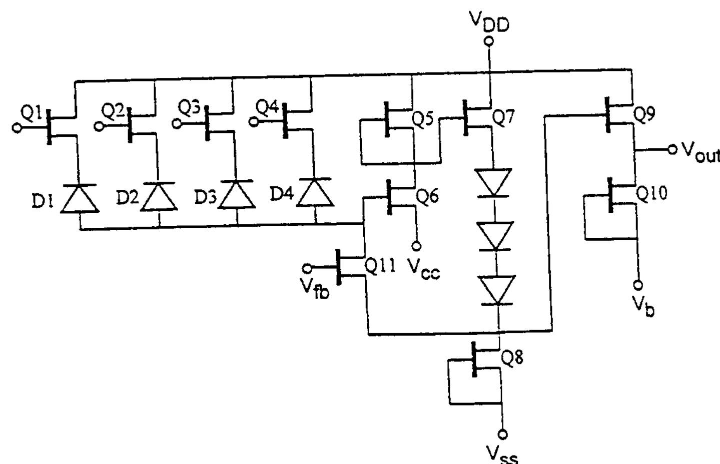


*Fig. 2: Schematic circuit diagram of the recently demonstrated 1x4 switchable detector/receiver array OEIC*

This technology can be considered as a versatile integration platform due to several features which are incorporated into the design: (i) There are no critical layer thickness dimensions or doping tolerances, (ii) there are no critical processing steps or device dimensions, (iii) the devices are all "planar" -- i.e. the diffused p-n junctions, formed in a single process step, are defined by windows pre-etched in a $SiN_x$ mask, (iv) there are only two basic circuit elements which are separately optimized in the grown structure: the p-i-n detector and the JFET/active load elements. This overall simplicity leads to very high yields and simple an accurate modeling of device performance prior to fabrication. The resulting circuits have been demonstrated to have good performance compared to other, more complex integration schemes as well as compared with hybrid receiver technologies. Finally, several different circuit codes can be simultaneously fabricated on these "standard"

wafer structures. For example, on a single MOCVD grown wafer, both the circuit in Fig. 2 as well as a coherent optical receiver were simultaneously fabricated with similar sensitivity performance and yield.

Using 2 x 50 μm gate geometries for Q1-Q8, the circuit had a 3 dB bandwidth of 1.1 GHz. Non-AR-coated p-i-n detectors had a dark current of 550 pA at -5V reverse bias and 50% quantum efficiency at a wavelength of $\lambda$=1.55μm. The detector isolation achieved by switching transistors Q1-Q4 was 60 dB. Finally, receiver sensitivity measured at 1 Gb/s using a non-return-to-zero coding format was -25 dBm at a bit error rate of 10-9 and $\lambda$ = 1.55μm (see Fig. 3). When the degradation due to lack of an AR coating is taken into account (approximately 2.5 dB), this sensitivity is comparable to the best demonstrated at this bit rate for an integrated, InP-based JFET optical receiver.

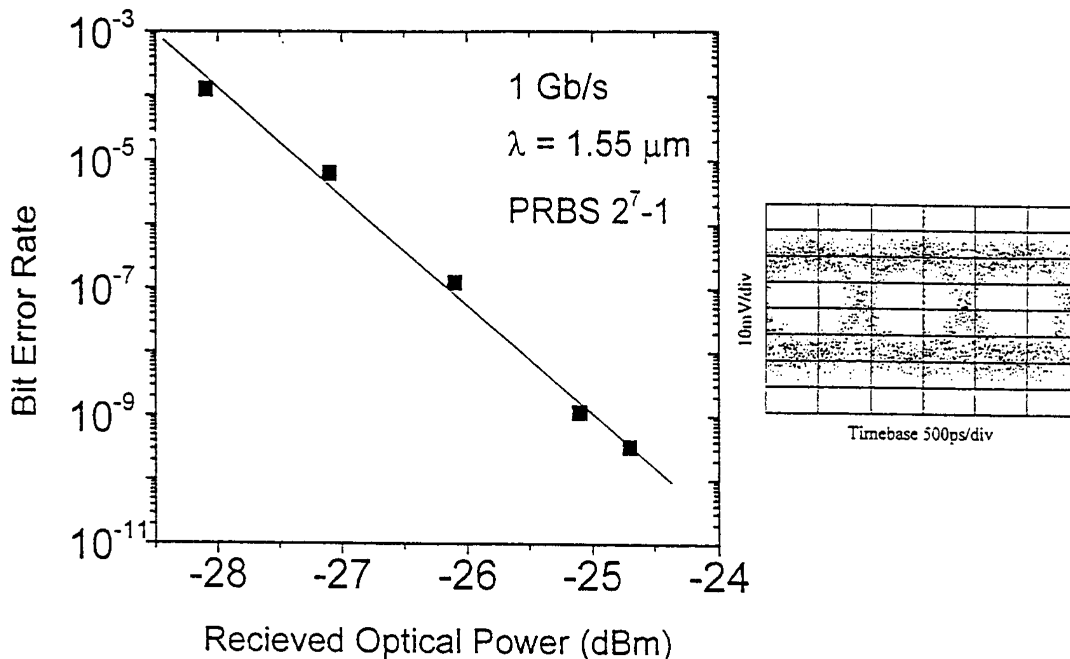


*Fig. 3: Bit error rate performance and eye pattern response (inset) of the receiver in Fig. 2 at 1 Gb/s and $\lambda$=1.55μm.*

A slight variation on the wafer structure shown in Fig. 1 was used to demonstrate[2] the largest InP-based OEIC reported to date: a 16x16 p-i-n detector/JFET switch focal plane array (FPA). The differences in the wafer and processing is that InGaAs channel was replaced by InP to reduce source-drain leakage, and a p+InP buffer layer was grown by gas source molecular beam epitaxy (GSMBE) between the SI:InP substrate and the channel layer, also to reduce leakage current. Furthermore, an additional Zn diffusion step was used around the JFET periphery down to the p+ buffer to increase JFET isolation without inducing further surface currents.

Using the circuit shown in Fig. 4, several different array sizes were fabricated, the largest (16x16) consisting of 528 active electronic devices and polyimide-isolated cross-over interconnects. An 8x8 version of the FPA is also shown in Fig. 4.

Also, there are no exposed p-n junctions, thus eliminating any surface leakage from the side walls of the JFET mesa. This structure also leads to improved yield since it eliminates any possibility of gate interconnect metallization shorting the device at the side walls. These features, coupled with the fact that lightly-doped InP was chosen as the channel material, resulted in discrete JFETs with drain leakage currents as low as 10 pA, which to our knowledge is at least a thousand-fold improvement over previous, conventional InP/InGaAs JFET leakage currents[7]. The typical dark current of the p-i-n diodes was 2 nA at 1V reverse bias, with external quantum efficiencies of $\eta = (0.7 \pm 0.05)$ at $\lambda = 1.3$ µm. The calculated noise equivalent power (NEP) for this array is 10-12 $W/cm^2\ Hz^{1/2}$, corresponding to a detectivity of $D^* = 5 \times 10^{14}$ cm $(Hz)^{1/2}/W$, using 100 MHz as the bandwidth and $4.6 \times 10^{-3}\ cm^2$ as the total FPA detection area. This value of D* is comparable to hybrid InGaAs FPAs, and at least two orders of magnitude higher than the HgCdTe FPAs at room temperature. The test of this technology as viable for use in LSI circuits based on InP is the total device yield. We found that 100% of the devices in the 8x8 and smaller arrays operated within pre-determined specifications, whereas only two devices (both JFETs) failed on the 16x16 array. This is equivalent to a 99.7% device yield, which is extremely high for any InP-based device technology, whether discrete or integrated.

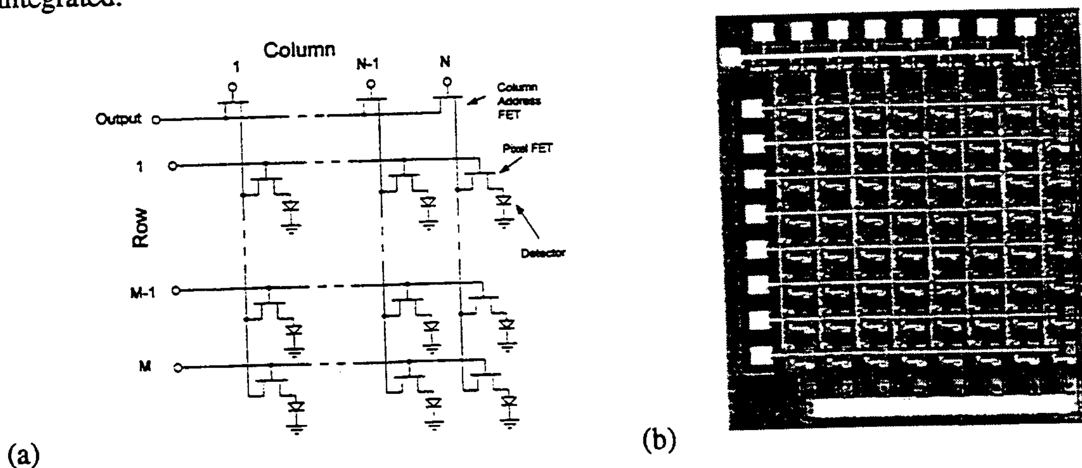


*Fig. 4: (a) Schematic circuit diagram of the FPA; (b) Micrograph of the 8x8 FPA measuring approximately 1mm².*

The two circuits described above are simple illustrations of the ease with which this p-i-n/JFET technology can be adapted to realize a wide range of receiver-based OEICs with bandwidths in the 1-5 GHz range, and with extremely high discrete device performance using a single, simple, versatile integration platform. Consistent with the integration platform concept, extremely high performance is sacrificed to the need to achieve a very high integration yield on standardized material structures. However, the performance of these example circuits is competitive with the best hybrid and monolithic receiver circuits reported using far more complex integration and design schemes.

## 3.0 TRANSMITTER PHOTONIC INTEGRATED CIRCUITS BASED ON TWIN WAVEGUIDE STRUCTURES

Photonic integrated circuits are generally employed for transmitter applications. Typically, they consist of a particular combination of active devices (lasers and SOAs), and passive devices (waveguides, modulators) to suit a given application. The competing materials requirements of the active and passive components typically resolved by employing

complex regrowth methods, where the active region of the devices are grown first, followed by etch-back and growth of a second set of layers used for the passive devices[8,9]. This regrowth technology is extremely difficult to control, and indeed has not been widely demonstrated using such processes as GSMBE. Furthermore, numerous materials issues must be addressed such as irregular interfaces at the regrown interfaces which can lead to poor device performance and high optical losses between adjoining devices.

This lead to our demonstration of a very simple, and flexible integration technology based on a modified twin waveguide (TG) structure to completely eliminate complicated regrowth processing. The basic concept of the TG structure is that an active MQW region is grown above a passive waveguide/modulator region, separated by an intermediate "cladding" region[10,11]. A laser or SOA is then defined in the active region by etching down into the clad. The difference between these two devices is simply the facet reflectivity: an SOA has anti-reflection coated facets, whereas a laser has high reflection coatings. To realize this device, we use very high quality facet formation processes based on $CH_4$:$H_2$ reactive ion etching[12].

The light generated in the active region is evanescently coupled into the passive, or waveguide region located directly below. As in any directional coupler, the coupling efficiency is a sensitive function of length. For this reason, previous TG structures[13] had a maximum coupling efficiency of 13%. To eliminate this length dependence, hence making the TG a practical integration scheme with no critical growth or processing tolerances, a thin (~100Å-200Å) InGaAs absorbing, or "loss" layer is placed in the center of the intermediate InP cladding layer. This loss layer is grown the length dependence of the coupling arises from an interplay between the odd and even modes propagating in the structure (see Fig. 5). Due to the different effective indices of the two modes, their velocities are different, and hence they are in and out of phase at different positions within the active cavity. The loss layer eliminates the even mode, hence eliminating this energy exchange with its concomitant length dependence.

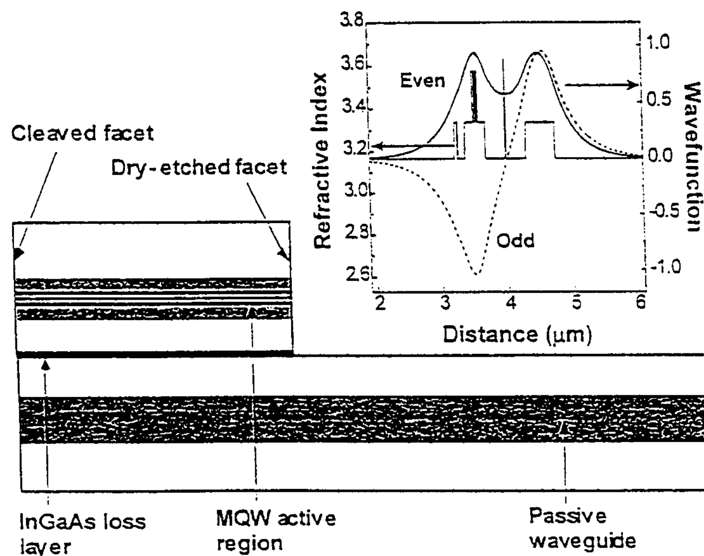


*Fig. 5: Schematic diagram of the TG structure with passive waveguide. Inset: Refractive index and calculated mode profiles in the TG structure with InGaAs loss layer.*

To test these assumptions, a laser coupled to a Y-branch waveguide at the output was fabricated (see Fig. 5). The difference between the structure tested and the multipurpose

platform wafer is that the lower passive waveguide shown in Fig. 5 is replaced by a large wavelength cutoff MQW waveguide section, and the wafer layers are grown starting from the p+InP substrate as follows (see Fig. 6): 1 μm thick p+InP cladding, InP/InGaAsP MQW waveguide region (approximately 10 periods, wavelength cutoff = 1.3μm), undoped InP cladding (thickness=0.5μm), InGaAs loss layer (thickness=100Å), undoped InP upper cladding (thickness=0.5μm), InP/InGaAsP MQW active region (3 to 5 periods, wavelength cutoff=1.55μm), p+InGaAsP cladding (thickness=0.5μm), p+InP cap/contact layer. The laser is biased by contacting the top p+InP cap and the lower, n-type cladding layers. To form a modulator, the cladding to substrate region is reverse biased. In this structure, facets are etched using 1:7 $CH_4$:$H_2$ plasma. The broad front facet shown in Fig. 6 is employed to eliminate damage to the laser ridge termination due to undercut etching. To reduce the reflectivity of SOA sections, the facets can be tilted away from 90° with respect to the waveguide longitudinal axis, in addition to being AR coated using SiO. Waveguide patterning is also accomplished by plasma etching of ridges.

In our laser/waveguide Y-junction device, no even mode propagation was detected, and as a consequence, there was no length dependence for the coupled radiation intensity. Indeed, a 50% coupling between the laser and the waveguide was measured. This is equal to the theoretical maximum coupling allowed in this structure, far exceeding all previous reports for coupling efficiency in such integrated devices, where a maximum 13% coupling has been reported for conventional TG structures[13]. One disadvantage of the TG structure is that the mode is shared with the waveguide, hence increasing the laser threshold current density by roughly a factor of two above that achieved using a conventional Fabry-Perot laser. To date, the minimum threshold current density measured in our 1.55μm wavelength, 3 active MQW TG structures is 700A/cm$^2$, which had a maximum output efficiency of 25%.

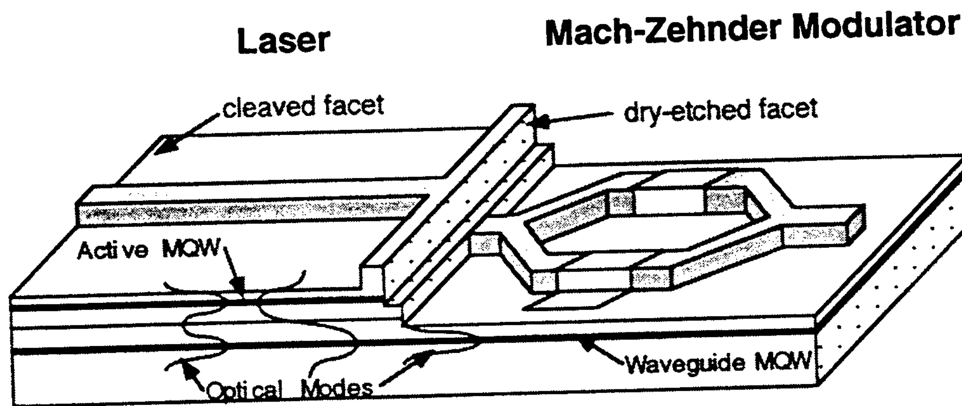


*Fig. 6: Laser/modulator PIC using the TG structure concept.*

Hence, the TG structure with loss layer provides a viable new approach to integrating passive and active optical devices on a single epitaxial wafer structure. This forms the basis of a practical "platform" PIC technology which is free from sensitivity to fabrication and epitaxial growth variations, and does not employ highly complex and costly regrowth methods. For the first time, we can look forward to generating a wide range of PICs on a single wafer, similar to what is accomplished using a single Si wafer to generate a wide range of integrated circuits and codes.

## 4.0 CONCLUSIONS

While the goal of generating a photonic integration technology with all the versatility and complexity available to Si VLSI is unrealistic, there is no question that steps taken in this direction will nevertheless lead to the widespread use of optics in systems which today cannot be attained due to the excessive costs and development times associated with fabricating complex photonic integrated circuits. The realization of such integration platforms will ultimately provide the system designer with a set of tools with which the time and costs to demonstrating new systems concepts can be drastically reduced. This ability has been one of the key features leading to the success of Si-based VLSI. The approaches discussed in this paper are intended to demonstrate some of the design and fabrication flexibility to photonics which are so readily available in to the electronic circuit designer.

## 5.0 ACKNOWLEDGMENTS

This paper is dedicated to the memory of Professor Walter Kosonocky who has been a long-time collaborator on this and other projects with many of the authors. We also thank the Office of Naval Research, DARPA and US Army CECOM whose support has made this work possible.

## 6.0 REFERENCES


1. K. Beyzavi, D. S. Kim, C. P. Chao, P. E. Burrows, and S. R. Forrest, IEEE Photonics Technology Lett.. **7,** 1162 (1995).
2. D. S. Kim, S. R. Forrest, M. J. Lange, G. H. Olsen, and W. Kosonocky, IEEE Photonics Technology Lett. **8,** 566-568 (1996).
3. D. C. W. Lo, Y. K. Chung, and S. R. Forrest, Photonics Technol. Lett. **2,** 675 (1990).
4. D. C. W. Lo, Y. K. Chung, and S. R. Forrest, IEEE Photonics Technol. Lett. **3**, 757 (1991).
5. D. C. W. Lo and S. R. Forrest, IEEE J. Lightwave Technol. **7,** 965 (1989).
6. S. Yu, K. J. Thomson, S. R. Forrest, E. Mykietyn, M. Lange, and G. H. Olsen, in A Monolithically Integrated 1x4 Switchable Photodiode Array with Preamplifier for Programmable Frequency Filters and Optical Interconnects, Boston, 1996, p. Paper PDP2.5.
7. D.-S. Kim, P. Studenkov, S. R. F. Lange, and G. H. Olsen, in Novel, 'p-encapsulated' InP JFETs with Very Low Leakage for Optoelectronic Integration with Infrared Focal Plane Arrays, Boston, 1996, p. Paper ThA4.
8. T. Sasaki, M. Yamaguchi, and M. Kitamura, J. Cryst. Growth **145,** 846 (1994).
9. L. Menigaux, D. Remiens, L. Dugrand, P. Sansonetti, and A. Carenco, in A New Monolithic Laser Waveguide Butt-Coupling Scheme Based on a Single-Step MOCVD, Boston, 1988, p. 172.
10. Y. Suematsu, M. Yamada, and K. Hayashi, Proc. IEE **63,** 208 (1975).
11. R. K. Watts, J. Appl. Phys. **44,** 5635 (1973).
12. C.-P. Chao, D. G. Garbuzov, G.-J. Shiau, and S. R. Forrest, IEEE Photonics Technology Lett. **7,** 836 (1995).
13. K. Utaka, Y. Suematsu, K. Kishino, and H. Kawanishi, Trans. IECE Japan **E62,** 319 (1979).